Biomedical Engineering Graduate Program
University of Brasília (UnB)
College of Sciences and Technologies in Engineering – FCTE/UnB

Simultaneous Positron Emission Tomography and Magnetic Resonance Image Reconstruction with Compressive Sensing using Cross-Prior Information and Pre-filtering

Gabriela Barbosa Silva

Advisor: Cristiano Jacques Miosso

University of Brasília
College of Sciences and Technologies in Engineering

Simultaneous Positron Emission Tomography and Magnetic Resonance Image Reconstruction with Compressive Sensing using Cross-Prior Information and Pre-filtering

Gabriela Barbosa Silva

Advisor: Cristiano Jacques Miosso

Master Degree Thesis on
Biomedical Engineering

Publication: 196A/2025

Brasilia/DF, January, 2025

University of Brasilia

College of Sciences and Technologies in Engineering

Graduate Program

Simultaneous Positron Emission Tomography and Magnetic Resonance Image Reconstruction with Compressive Sensing using Cross-Prior Information and Pre-filtering

Gabriela Barbosa Silva

Master Thesis submitted to the Biomedical Engineering Graduate Program, as a partial fulfillment of the requirements for the degree of Master in Biomedical Engineering

Approved by:

Cristiano Jacques Miosso

(Advisor)

Dr. Fabiano Araujo Soares

(Internal examiner)

Dr. Alexsandro Eurípedes Ferreira

(External examiner)

Brasilia/DF, January, 2025

Catalog Card

Barbosa Silva, Gabriela
Simultaneous Positron Emission Tomography and Magnetic Resonance Image Reconstruction with Compressive Sensing using Cross-Prior Information and Pre-filtering
Distrito Federal, 2025.
76p., 210 × 297 mm (FGA/UnB Gama, Mestrado em Engenharia Biomédica, 2025).
Dissertação de Mestrado em Engenharia Biomédica, Faculdade de Ciências e Tecnologias em Engenharia, Programa de Pós-Graduação em Engenharia Biomédica.

1. PET/MRI
2. Medical Imaging
3. Compressive Sensing
4. Image Reconstruction

I. FGA UnB/UnB.
II. Título (série)

Reference

Barbosa Silva, Gabriela (2025). Simultaneous Positron Emission Tomography and Magnetic Resonance Image Reconstruction with Compressive Sensing using Cross-Prior Information and Pre-filtering. Master thesis in Biomedical Engineering, Publication 196A/2025, Biomedical Engineering Graduate Program, University of Brasilia at Gama, Brasilia, DF, 76p.

Copyright

---

bsgabieng@gmail.com

Brasília, DF – Brasil

Acknowledgments

This study was financed in part by the Coordenação de Aperfeiçoamento de Pessoal de Nível Superior - Brasil (CAPES) – Finance Code 001.

Imagens de Tomografia por Emissão de Pósitrons e Ressonância Magnética Simultâneas com Compressive Sensing usando Informação a Priori Cruzada e Pré-filtragem

Resumo Estendido

A tecnologia de tomografia por emissão de pósitrons combinada com imagem de ressonância magnética (PET/MRI) constitui uma modalidade de imagem relativamente nova que combina a capacidade do PET de rastrear o metabolismo com a resolução espacial da Ressonância Magnética (MR).

Esta pesquisa utiliza informação a priori (IP) extraída de dados de imagens de PET, que foram adquiridas simultaneamente com a RM do equipamento da Siemens® de PET/MRI, *Biograph mMR*. É explorado o fato de que as imagens de PET e de RM são adquiridas simultaneamente para usar informações da modalidade de PET com *Compressive Sensing* (CS) para melhorar a reconstrução das imagens de RM.

A metodologia foi testada variando o percentual de coeficientes da representação esparsa considerada como posições de elementos não nulos (e, portanto, usada como IP) de 0 a 90 %, com 10 valores igualmente espaçados e variando o número de ângulos usados na trajetória radial da ressonância magnética de 10 a 160 ângulos, com 7 valores igualmente espaçados.

A qualidade das imagens foi avaliada quantitativamente, utilizando as métricas de *signal-to-error-ratio* (SER) e *Structural Similarity Index Measure* (SSIM) para avaliar a qualidade das imagens. As opiniões de especialistas em radiologia não foram coletadas para sustentar uma análise qualitativa. Com uma proporção de IP de 10 %, a qualidade das imagens reconstruídas melhora em comparação com aquelas reconstruídas sem IP para todas as faixas de ângulos testados.

Palavras-chave: PET/MRI, Compressive Sensing, Reconstrução de Imagem, Informação a Priori

1 Introdução

Os *scanners* tomografia por emissão de pósitrons acoplados aos de ressonância magnética (PET-MR) combinam a capacidade do PET de rastrear o metabolismo com a resolução da RM na análise de tecidos moles [126].

Os equipamentos de PET/MRI utilizam uma dose de radiação menor em comparação com a Tomografia por Emissão de Pósitrons com Tomografia Computadorizada (PET/CT) [158]. Entretanto, os exames podem levar mais tempo do que os de RM e PET/CT devido à ne-

cessidade de adquirir imagens detalhadas de ambas as modalidades [135].

O aumento dos tempos de aquisição pode levar a maiores riscos de movimentos involuntários do paciente, causando artefatos de movimento [3]. Além dos artefatos originados por movimentos de pacientes, o *hardware* de ambos os *scanners* causa interferência entre si, resultando em atenuação nas imagens [3, 107, 192].

Esta pesquisa propõe e desenvolve um método para reconstrução de imagens de PET/MRI que explora informação a priori (IP) extraída de imagens de PET com CS e pré-filtragem para melhorar a qualidade das imagens de RM. Argumenta-se que este método pode reduzir os efeitos da atenuação do PET/MRI e o número de medidas necessárias para atingir uma determinada qualidade objetiva de imagem.

Ao contrário dos métodos tradicionais que exigem a aquisição de um conjunto de dados completo, o CS permite a reconstrução de imagens de alta qualidade com um número de medidas significativamente menor [180].

Após os desenvolvimentos iniciais do CS, os avanços teóricos e empíricos subsequentes levaram a reduções ainda maiores do número de medidas necessárias para atingir uma qualidade de imagem estabelecida. Um dos avanços teóricos mais importantes é o uso de IP. A incorporação de IP na reconstrução de imagens com CS pode melhorar os resultados, levando a imagens com maior resolução espacial, menor ruído e melhor fidelidade à imagem original [180, 116].

Este trabalho procura explorar o fato de que as imagens são adquiridas simultaneamente para usar IP de imagens de PET e CS para reconstruir imagens de RM e melhorar a qualidade da imagem. No PET/MRI já foi feito o uso de IP de uma modalidade para outra a partir de uma regularização generalizada da esparsidade articular [112], como um dicionário conjunto baseado em PET/MRI modelado como um campo aleatório de Markov para reconstrução bayesiana [166], com dados aleatórios borrados do domínio de Fourier subdeterminados por PET com ruído gaussiano de MRI [50]. Mas não foi encontrado na literatura o uso de IP da mesma posição de corte de uma modalidade para outra com CS e pré-filtragem.

2 Fundamentação teórica e estado-da-arte

O imageamento médico, é uma especialidade que usa tecnologias para criar imagens do interior do corpo humano para fins de diagnóstico. Essas imagens fornecem aos profissionais da área da saúde informações valiosas sobre a anatomia, fisiologia e função de órgãos e tecidos, ajudando-os a diagnosticar doenças, planejar tratamentos e monitorar respostas terapêuticas [4].

Este trabalho se concentrará em imagens de RM e de PET. O primeiro usa um forte campo magnético e ondas de radiofrequência (RF) para criar imagens detalhadas de órgãos e tecidos [173] e é usado para diagnosticar doenças do cérebro [24], tumore, entre outras

doenças [92]. O segundo usa radioisótopos injetados no corpo do paciente, que se acumulam em áreas com alto metabolismo, como tumores ou áreas de inflamação [12]. Os exames de PET ajudam a diagnosticar tumores [23], infecções e distúrbios neurológicos [130].

As imagens de PET/MRI são adquiridas simultaneamente, permitindo uma análise detalhada da anatomia e da atividade metabólica. Em comparação com a Tomografia por Emissão de Pósitrons com a Tomografia Computadorizada (PET/CT), o PET/MRI elimina a exposição à radiação ionizante da TC [158], tornando-a uma opção mais segura. As imagens fornecem uma diferenciação mais precisa entre tumores e inflamação e melhor diferenciação de tecidos moles [110, 80].

O sistema do PET compreende um anel de detectores cintilantes que capturam os fótons gama emitidos pelos radioisótopos injetados no paciente. Tradicionalmente, o design dos sistemas de PET utiliza tubos fotomultiplicadores (PMT). No entanto, os PMT são altamente suscetíveis até mesmo a pequenos campos magnéticos [198].

A RM usa três tipos de campos magnéticos gerados por três tipos de bobinas: campo magnético estático, campo magnético gradiente e campo de radiofrequência. No entanto, os circuitos *front-end* (F/E) do PET são propensos a interferências de RF. Por isso os sistemas de *scanner* de PET causam alterações no campo magnético homogêneo da RM [6].

A atenuação da imagem pode levar à perda de resolução espacial e distorção da imagem do PET, dificultando a interpretação dos resultados. A atenuação não-uniforme dos raios gama pode levar à estimativa da atividade metabólica incorreta [172]. Técnicas de correção de atenuação minimizam o impacto desse fator na imagem de PET [131].

O CS propõe um paradigma para a aquisição de dados, permitindo a reconstrução de sinais a partir de um número reduzido de amostras, menor do que a quantidade exigida pela abordagem de Nyquist-Shannon. Imagine um sinal unidimensional x com tamanho N. É possível reconstruir x com um número l de medidas, onde

$$l < N, \tag{1}$$

se x tiver uma representação esparsa em um domínio conhecido.

Em outras palavras, se três condições forem atendidas, é possível calcular um sinal x_{Nx1} a partir de x $l < N$ medidas lineares. A primeira é que

$$\hat{x} = Tx, \tag{2}$$

onde $\hat{x}$ é a representação esparsa de x e T é um domínio conhecido. A segunda condição é que l não pode ser menor que o limite de dispersão, mas deve ser menor que N. A última condição é que o processo de medição seja incoerente com T.

Por esse motivo, procuramos obter um x dado por

$$Mx = b, \tag{3}$$

onde M é a matriz de medidas e b representa o sinal l componentes diferentes de zero. A equação 3.13 tem infinitas soluções. Devemos escolher o mais esparso. Idealmente

$$\hat{x}^* = argmin_{\hat{x}} \left\| \hat{x} \right\|_0, \tag{4}$$

de tal forma que

$$MT^{-1}\hat{x} = b, \tag{5}$$

e

$$x^* = T^{-1}\hat{x}^*, \tag{6}$$

onde T é a transformação esparsificante. Esta solução tem complexidade combinatória porque, para resolvê-la, devemos testar todas as posições possíveis de elementos não-nulos e, para cada um, ver se o sistema reduzido correspondente aceita solução. Depois disso, escolhemos o mais esparso.

A transformação esparsificante representa o sinal original em uma representação esparsa em um determinado domínio. Essa transformação busca uma base de representação onde relativamente poucos componentes diferentes de zero podem representar o sinal original. Várias transformações podem ser usadas como transformações esparsificantes em CS, por exemplo, transformadas de Fourier e *Wavelet*.

No entanto, a aplicação de transformações esparsas pode aumentar a complexidade computacional dos algoritmos de CS, particularmente para grandes conjuntos de dados. Para isso, a pré-filtragem pode ser uma técnica útil. A pré-filtragem consiste em aplicar um filtro ao sinal original [179].

Outra ferramenta pode ser usada para ajudar a otimizar o processo de reconstrução com CS, é o uso de IP que é o conhecimento prévio sobre o sinal adquirido. Essas informações podem ajudar a limitar o conjunto de soluções possíveis para a reconstrução do sinal, facilitando o processo e aumentando a precisão [118]. Essas informações podem ser da estrutura do sinal, natureza, estatísticas ou dados relacionados.

No PET/MRI, a IP fornece uma máscara que restringe a reconstrução da imagem de PET a partir de informações anatômicas obtidas pela de MRI. Ele também pode fornecer informações como densidade e composição do tecido das imagens de RM na reconstrução de imagens de PET [193].

Em [163], foi observado que é possível extrair IP de uma modalidade para outra de PET/MRI, o programa utilizado foi desenvolvido para imagens PET/CT em [58]. O uso de IP combinado com técnicas de reconstrução de imagens pode melhorar o processo e, ao

mesmo tempo, acelerá-lo [87].

Existem técnicas de imagem que fazem uso de IP, extraindo informações de um corte para outro [58] ou de um *frame* para outro [116]. Em [113], IP anatômica de MRI é usado para reconstruir imagens PET adquiridas de um equipamento PET/MRI, e o uso de CS para a metodologia é avaliado. No estudo, o método CS teve um bom desempenho na redução de artefatos. Ainda assim, não apresentou bons resultados na correção de artefatos causados pelo movimento e teve um alto custo computacional. No entanto, o autor sugere que mais investigações podem ser feitas otimizando o algoritmo CS.

3 Materiais e Métodos

Os dados foram extraídos da máquina *Biograph mMR* da Siemens ®. Para encontrar os pares de imagens foi feito um programa para acessar os metadados das imagens. Primeiro, o algoritmo separa as imagens por estudos e forma os pares por proximidade de corte. Uma vez formados os pares, as imagens foram alinhadas manualmente.

Este trabalho aborda o desenvolvimento e avaliação de um sistema de análise de imagens IP de imagens de PET utilizadas na reconstrução de imagens de RM. Em um cenário de medições em que as imagens de PET e de RM foram adquiridas simultaneamente. A ideia é avaliar se há melhora na reconstrução da RM com base nas medidas de PET obtidas na mesma condição de posição, anatomia e fisiologia, em comparação com o cenário usual em que cada imagem é reconstruída isoladamente das medidas correspondentes a cada caso.

Para tanto, é proposto um conjunto de algoritmos que começa a extração de IP das imagens de PET. A partir dessas imagens, um conjunto de posições de elementos não-nulos são extraídos na representação esparsa para ser usado na próxima etapa. A sequência é realizada aplicando técnicas de CS usando as medidas lineares da RM.

A ideia é explorar as informações já obtidas a partir de imagens de PET e observar a qualidade da reconstrução dependendo do número de posições extraídas e do número de medidas utilizadas. A expectativa é que o uso de IP de imagens PET para imagens de RM leve a um aumento estatisticamente significativo na qualidade objetiva das imagens de RM, refletindo um ganho potencial para a modalidade de PET/MRI devido ao equipamento permitir a aquisição simultânea de medidas de PET e de RM.

Para cada imagem de RM fornecida pela SIEMENS®, diferentes conjuntos de medidas foram inicialmente extraídos do espaço-k para avaliar a reconstrução com CS em diferentes cenários (com e sem IP de imagens de PET). Neste experimento, consideramos a trajetória radial para extrair as medidas, o que é um bom compromisso entre qualidade e complexidade.

Para simular as medidas da máquina RM, foi implementada uma função Python que, com base nas dimensões da imagem e nos vários ângulos de inclinação entre as linhas radiais, retorna as posições dos pontos ao longo da trajetória. Em outras palavras, essa função

retorna as posições das informações que a máquina RM forneceria ao longo da trajetória.

Os ângulos de inclinação são igualmente espaçados, variando de 0 a π. Eles determinam o número de linhas radiais que a trajetória terá. Após isso, calcula-se a transformada discreta de Fourier (DFT) da imagem de RM e fazemos medições apenas nos pontos da trajetória radial.

Foi avaliada a qualidade objetiva das imagens reconstruídas com 7 ângulos variados em uma faixa de 10 a 160. Quanto menos ângulos, menor o tempo de reconstrução. No entanto, a qualidade da imagem é comprometida. Avalia-se se o uso de CS melhora a qualidade da imagem, mesmo em um número baixo de ângulos.

De acordo com [179], o processo de pré-filtragem é benéfico para o processo de reconstrução do ponto de vista da qualidade e do tempo da reconstrução. Como resultado desta operação, três imagens são obtidas. Cada uma delas representa informações de alta frequência em uma direção. Dessa forma, uma tem uma imagem esparsa com altas frequências na horizontal, outra na vertical e outra na diagonal. O nível DC é representado pelas informações de trajetória obtidas do *scanner* de RM.

Nesse caso, cada versão filtrada da imagem é sua representação esparsa. Já foi demonstrado em [179] que, se informações adicionais sobre o domínio esparso de suporte forem obtidas, menos amostras no domínio do tempo serão necessárias.

Essas informações são extraídas das imagens de PET obtendo os valores de espectro mais altos. Em outras palavras, a DFT das imagens de PET é calculada e, em seguida, o espectro 2D é empilhado em um espectro 1D. Após esse processo, os sinais são classificados de forma decrescente e, finalmente, os sinais mais altos são obtidos.

O processo de reconstrução é realizado após a obtenção do IP e das três imagens decompostas. Como as três representações são independentes, elas podem ser reconstruídas em paralelo. O resultado é obtido aplicando uma composição espectral das imagens.

Uma das hipóteses a serem investigadas era se a extração de IP de imagens PET para reconstruir imagens RM com CS permitiria o processo de reconstrução com menos medidas. Dessa forma, foram feitas alterações no número de medidas e avaliada a qualidade da imagem reconstruída.

Para avaliar a qualidade das imagens, foram utilizadas a SER e a SSIM. As métricas foram coletada para cada cenário. Além disso, foi observado o efeito da quantidade de IP extraída das imagens de PET sobre o resultado. Foram feitos testes para 10 porcentagens de IP, em todos os casos de diferentes quantidades de medidas da RM.

Usamos o teste de Wilcoxon para amostras pareadas. O valor de p foi calculado para avaliar a significância estatística da diferença entre as médias. Em seguida, o valor de p

obtido foi comparado com o nível de significância pré-definido de 0,05.

4 Resultados e Discussões

Com este estudo, é pretendido responder à seguinte pergunta: "Qual a SER e SSIM obtidas quando aplicados IP a partir de imagens PET combinadas com algoritmos CS para reconstruir imagens RM?".

A relevância dessa pergunta reside na necessidade de reduzir o número de medidas necessárias para a reconstrução de imagens de RM, reduzir o tempo de aquisição e melhorar a qualidade das imagens, mitigando a interferência de ruído na imagem reconstruída. Os resultados obtidos nesta pesquisa demonstram uma correlação positiva entre o uso de IP no processo de reconstrução de imagens RM e o aumento da qualidade da imagem, corroborando os achados em [116].

O conjunto de dados tem 448 pares de imagens PET e RM de várias posições de corte de uma cabeça humana. A reconstrução foi aplicada nas primeiras 100 imagens. Para cada imagem, o processo de reconstrução foi realizado com diferentes números de linhas radiais e, para cada número de linhas radiais, uma porção diferente de IP. Para o experimento, foi utilizado um intervalo de ângulos de linhas radiais entre 10 e 160 com um intervalo de 25, e um intervalo de 0 a 90 % de IP com um intervalo de 10 %. As figuras 5.2 e 5.3 contém os valores médios de SER e SSIM para as amostras em todos os cenários do experimento.

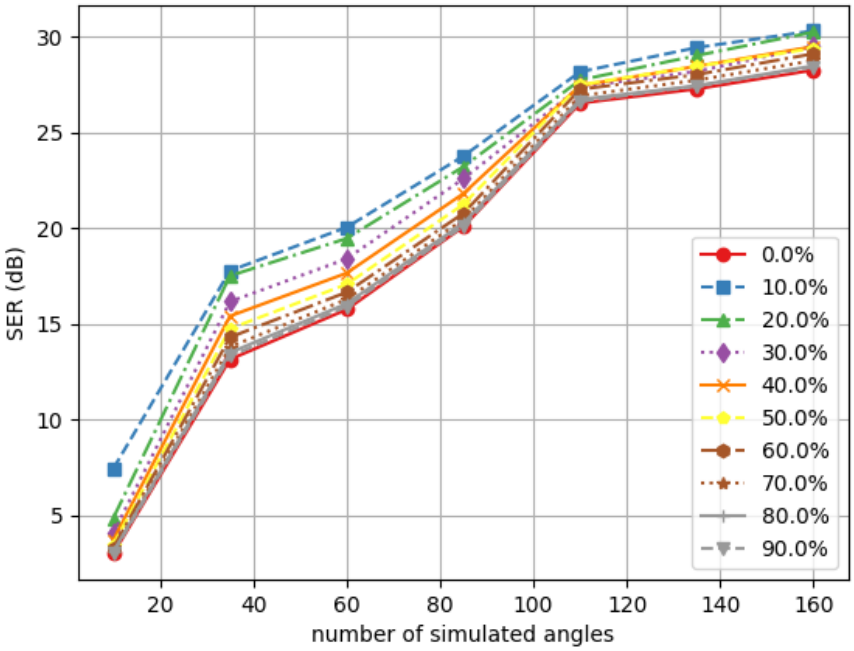

Figura 1. Os valores médios de SER de 100 imagens para 7 números diferentes de ângulos igualmente distribuídos entre 10 e 160. Para cada número de ângulos, o experimento foi reproduzido para diferentes proporções de IP, de 0 a 10 %. As imagens reconstruídas com 10 % de IP tiveram a melhor SER.

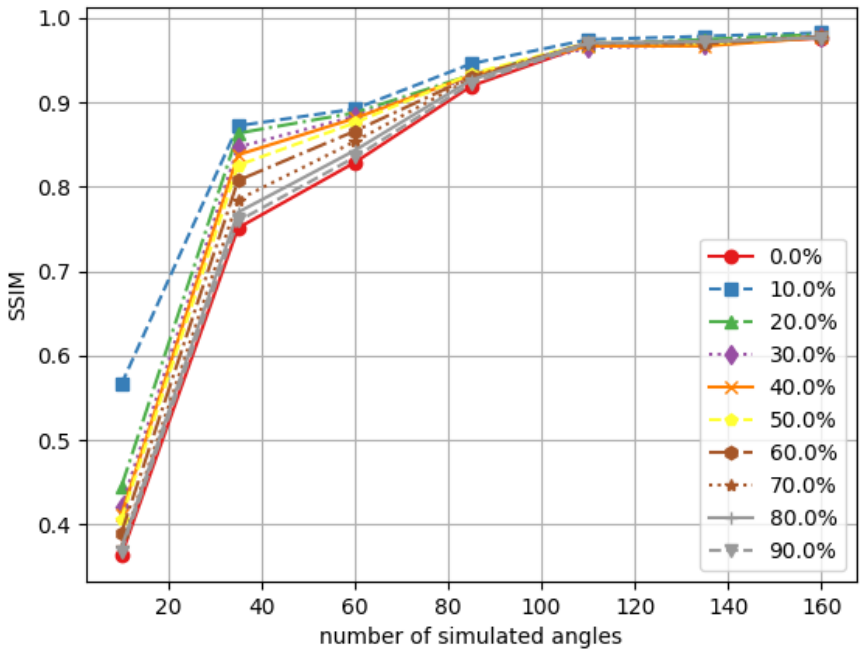

Figura 2. Os valores médios de SSIM de 100 imagens para 7 números diferentes de ângulos distribuem igualmente entre 10 e 160. Para cada número de ângulos, o experimento foi reproduzido para diferentes proporções de IP, de 0 a 10 %. As imagens reconstruídas com 10 % de IP tiveram a melhor SSIM.

Para avaliar o impacto da alteração do número de ângulos e da proporção IP na SER e na SSIM, utilizou-se o teste de Wilcoxon. A hipótese nula (H0) pressupôs que não haveria diferença significativa entre as medidas antes e depois da intervenção. Considerando um nível de significância de $p \leq 0,05$, rejeitamos a hipótese nula, que indica que a intervenção causou uma diferença estatisticamente significativa de SER e SSIM. Esses resultados sugerem que a nova intervenção foi eficaz na melhoria da qualidade da imagem e, ao mesmo tempo, na redução do número de medidas necessárias para a reconstrução de imagens de RM usando IP de imagens de PET adquiridas simultaneamente.

A partir dos resultados, é possível inferir que o uso de informações IP de imagens de PET em algoritmos com CS pode reduzir o número de medidas necessárias para reconstruir imagens de RM. De acordo com a Figura 5.3, com 85 ângulos, podemos obter um SSIM maior que 0,9 e após 100 ângulos, o valor de SSIM atinge seu ponto de saturação. Na Figura 5.8, podemos observar esse resultado do ponto de vista qualitativo.

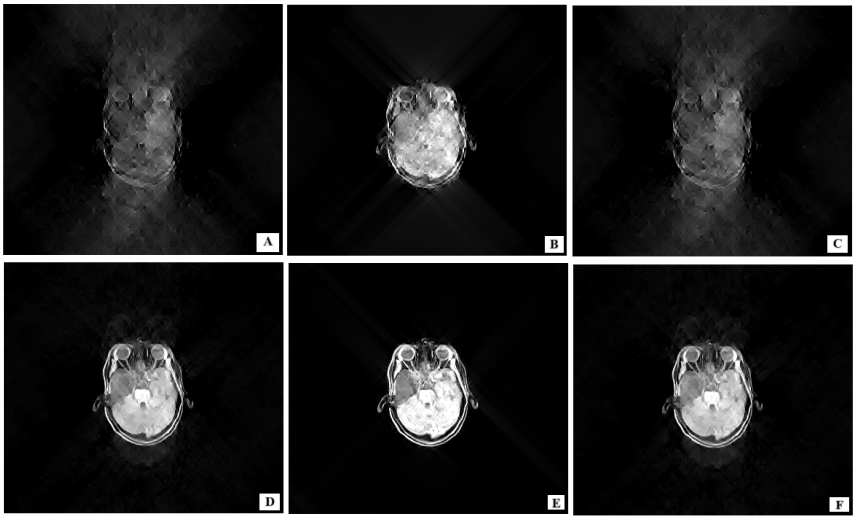

Figura 3. Comparação de diferentes cenários. As figuras A, B e C são imagens reconstruídas com 10 ângulos com 0 %, 10 % e 90 %de IP. As figuras D, E e F são imagens reconstruídas com 35 ângulos e 0 %, 10 %, e 90 % de IP. É possível observar uma melhora na qualidade entre as Figuras A e B, embora as imagens ainda tenham baixa resolução. Na Figura C, fica claro que houve uma queda na qualidade da imagem. As Figuras D, E e F melhoram significativamente a resolução, com a Figura E tendo maior qualidade visual. Isso apoia a hipótese de que imagens com 10 % de IP apresentam melhores resultados.

O valor de 10 % de IP é a proporção que mostrou os melhores resultados. Usando 10 % de IP de imagens de PET, podemos obter pelo menos 0,9 de SSIM com 80 ângulos de linhas radiais da RM. Com mais de 100 ângulos, o SSIM atinge seu ponto de saturação, conforme observado na Figura 5.7.

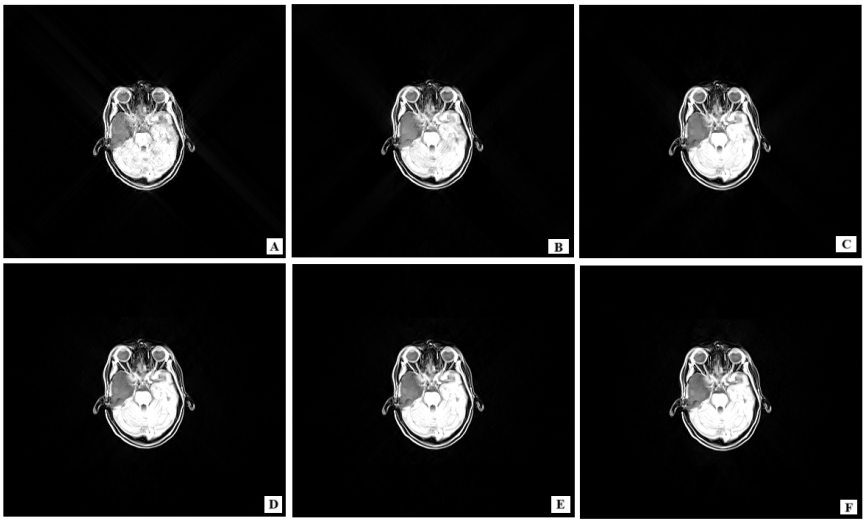

Figura 4. Imagens reconstruídas com 10 % de IP para diferentes ângulos. As Figuras A a F são as imagens RM reconstruídas com o intervalo de 35 a 160 ângulos igualmente espaçados. É possível notar que da Figura C a F as imagens são muito semelhantes.

Os resultados demonstram que o uso de 10 % de IP melhora objetivamente a qualidade das imagens e reduz o número de medidas necessárias para a reconstrução. Esses resultados corroboram os de estudos anteriores em que o uso de IP combinado com CS pode melhorar a qualidade da imagem. No entanto, um valor muito alto de IP pode reduzir a qualidade das imagens. Isso pode estar relacionado ao fato de que uma quantidade muito alta de IP pode trazer ruído inerente à imagem de suporte.

5 Conclusão

A presente pesquisa explora o potencial da incorporação de IP de imagens de PET no processo de reconstrução de imagens de RM usando CS e pré-filtragem. Esse método ajuda na reconstrução porque as imagens de PET são extraídas da mesma posição de *frame* e corte que as imagens de RM.

A hipótese central era de que o uso de IP de imagens de diferentes modalidades extraídas simultaneamente da mesma posição e orientação de corte poderia melhorar a qualidade da imagem reconstruída. No caso do PET/MRI, isso pode compensar o ruído causado por interferências inerentes ao equipamento e reduzir o número de medidas utilizadas no processo de reconstrução.

Uma simulação do espaço-k foi extraída das imagens originais, com o número de ângulos correspondentes ao cenário a ser avaliado no experimento, para obter a trajetória radial das imagens de ressonância. Esse resultado foi filtrado com filtros de Haar, e cada uma das três versões obtidas foi reconstruída usando CS com minimização l_p, com p = 1 e com IP extraído das imagens PET correspondentes à mesma posição de corte. Ao final desse processo, foram obtidas três imagens esparsas, e a imagem final foi formada através de uma composição espectral das três imagens.

Foram realizados experimentos com 100 imagens em diferentes cenários. Os resultados da reconstrução foram testados variando a porcentagem de IP de 0 a 90 %, com 10 valores igualmente espaçados, e o número de ângulos de 10 a 160, com 7 valores igualmente espaçados. Usamos a relação sinal-ruído (SER) e a medida do índice de similaridade estrutural (SSIM) para avaliação da qualidade da imagem.

Os resultados mostraram que o uso de 10 % de IP melhorou a qualidade da imagem para todos os cenários. As imagens reconstruídas com 60 ângulos tinham um SER médio de aproximadamente 16dB e um SSIM médio de aproximadamente 0,82, enquanto as imagens reconstruídas com 10 % de IP tinham um SER médio de 20dB e um SSIM médio de aproximadamente 0,89.

Em resumo, os resultados demonstraram que o uso de 10 % de IP de imagens de PET pode reduzir o número de medidas necessárias para o processo de reconstrução e melhorar a qualidade das imagens de RM. Esses resultados corroboram os de estudos anteriores que apontam que o uso de IP pode melhorar a qualidade das imagens reconstruídas e revelam

que um número elevado de IP pode impactar negativamente a qualidade das imagens.

Pesquisas futuras podem explorar análises sobre o tempo de processamento e o processo de otimização ou experimentos para uma porcentagem de IP acima de 90 %. Se a qualidade das imagens piorar o resultado sem IP, pode ser um indicativo de que a porcentagem de coeficientes nas imagens de PET representa menos conteúdo do que em outros tipos de imagem. Outro ponto é testar as porcentagens de IP entre 10 % e 20 % com espaçamento menor entre os valores. Há também a necessidade de investigar essa metodologia com outros métodos de pré-filtragem, trajetória e regiões anatômicas. O uso de inteligência artificial para extrair IP de forma mais eficaz também pode ser avaliado: altos coeficientes sempre podem trazer pelo menos uma pequena porcentagem de ruído.

Em suma, os resultados deste estudo contribuem para uma melhor compreensão de como o uso de IP de uma modalidade para outra pode impactar o processo de reconstrução de imagens com CS.

Lista de Referências

[1] A. Afaq, D. Faul, V. V. Chebrolu, e et al. Pitfalls on pet/mri. *Seminars in Nuclear Medicine*, 51(5):529–539, 2021.

[2] B. Aggarwal. *Textbook of Radiology and Imaging, Volume 1-E-Book*. Elsevier India, 2023.

[3] M. S. H. Akram, T. Obata, M. Suga, e et al. Mri compatibility study of an integrated pet/rf-coil prototype system at 3 t. *Journal of Magnetic Resonance*, 283:62–70, 2017.

[4] S. Basu, S. Hess, P. N. Braad, e et al. The basic principles of fdg-pet/ct imaging. *PET clinics*, 9(4):355–370, 2014.

[5] M. J. Ehrhardt, K. Thielemans, L. Pizarro, e et al. Joint reconstruction of pet-mri by exploiting structural similarity. *Inverse Problems*, 31(1):015001, 2014.

[6] Y. Garcia, C. Franco, e C. J. Miosso. Method for improved image reconstruction in computed tomography and positron emission tomography, based on compressive sensing with prefiltering in the frequency domain. páginas 2019–2025, 2020.

[7] H. Jadvar e P. M. Colletti. Competitive advantage of pet/mri. *European journal of radiology*, 83(1):84–94, 2014.

[8] R. Kang, D. Ai, G. Qu, e et al. Prior information constrained alternating direction method of multipliers for longitudinal compressive sensing mr imaging. *Neurocomputing*, 376:128–140, 2020.

[9] V. Kuperman. *Magnetic resonance imaging: physical principles and applications*. Elsevier, 2000.

[10] J. E. Mackewn, J. Stirling, S. Jeljeli, e et al. Practical issues and limitations of brain attenuation correction on a simultaneous pet-mr scanner. *EJNMMI physics*, 7(24):1–17, 2020.

[11] M. E. Mayerhoefer, H. Prosch, e L. Beer. Pet/mri versus pet/ct in oncology: a prospective single-center study of 330 examinations focusing on implications for patient management and cost considerations. *Springerlink*, 47(1):51–60, 2019.

[12] A. Mehranian, M. A. Belzunce, C. Prieto, e et al. Synergistic pet and sense mr image reconstruction using joint sparsity regularization. *IEEE transactions on medical imaging*, 37(1):20–34, 2017.

[13] B. G. Mersereau. *MRI-Guided and Compressed Sensing Reconstruction Methods for PET/MRI.* Doctoral dissertation, Graduate Faculty of North Carolina State University, 2017.

[14] C. J. Miosso, R. von Borries, M. Argaez, e et al. Compressive sensing reconstruction with prior information by iteratively reweighted least-squares. *IEEE Transactions on Signal Processing*, 57(6):2424–2431, 2009.

[15] C. J. Miosso, R. von Borries, e J. H. Pierluissi. Compressive sensing with prior information: Requirements and probabilities of reconstruction in l1 -minimization. *IEEE transactions on signal processing*, 61(9):2150–2164, 2013.

[16] S. Musafargani, K. K. Ghosh, S. Mishra, e et al. Pet/mri: a frontier in era of complementary hybrid imaging. *European journal of hybrid imaging*, 2(12):1–28, 2018.

[17] R. Ni. Pet imaging in animal models of parkinson's disease. *Behavioural Brain Research*, 438:114174, 2023.

[18] R. Nutt e M. A. King. Pet/mri: A dream come true? *The Lancet*, 376(9742):1199–1209, 2010.

[19] L. Pang, Z. Zhang, G. Liuand, e et al. Comparison of the accuracy of a deep learning method for lesion detection in pet/ct and pet/mri images. *Molecular Imaging and Biology*, 26(5):802–811, 2024.

[20] T. Sepehrizadeh, I. Jong, M. DeVeerand, e et al. Pet/mri in paediatric disease. *European journal of radiology*, 144:109987, 2021.

[21] G. B. Silva. *Avaliação de extração de informação a priori entre imagens de diferentes modalidades para aprimoramento de reconstrução de imagens médicas em equipamentos de PET-MRI*. Trabalho de conclusão de curso, Graduação em Engenharia Eletrônica, Universidade de Brasília, Campus Gama, 2020.

[22] V. P. Sudarshan, G. F. Egan, Z. Chen, e et al. Joint pet-mri image reconstruction using a patch-based joint-dictionary prior. *Medical image analysis*, 62:101669, 2020.

[23] M. Sun, G. Feng, L. Peng, e X. Gao. Correlation between ivim histogram parameters and 18f-fdg pet metrics in hepatic tumors: A retrospective study. *Journal of Nuclear Medicine*, 61, 2020.

[24] B. Sundermann, B. Billebaut, J. Bauer, e et al. Practical aspects of novel mri techniques in neuroradiology: Part 2 – acceleration methods and implications for individual regions. *RöFo - Fortschritte auf dem Gebiet der Röntgenstrahlen und der bildgebenden Verfahren*, 194:1195–1203, 2022.

[25] S. T. Treves e M. Pomper. Pet/mri: A review of the clinical literature. *Journal of Nuclear Medicine*, 51(12):182–1834, 2010.

[26] R. M. van Geuns, P. A. Wielopolski, H. G. de Bruin, e et al. Basic principles of magnetic resonance imaging. *Progress in cardiovascular diseases*, 42:149–156, 1999.

[27] J. Vivian. *Compressive sensing using directional filters for Magnetic Resonance Image reconstruction under different k-space trajectories*. Dissertação de mestrado, Programa de Pós-Graduação em Engenharia Biomédica, Universidade de Brasília, Campus Gama, 2020.

[28] R. von Borries, C. J. Miosso, e C. Potes. Compressed sensing using prior information. In *2007 2nd IEEE International Workshop on Computational Advances in Multi-Sensor Adaptive Processing*, páginas 121–124. IEEE, 2007.

[29] J. Won, J. Yeon, H. Park, , e et al. Development and initial results of a brain pet insert for simultaneous 7-tesla pet/mri using an fpga-only signal digitization method. *IEEE Transactions on Medical Imaging*, 40(6):1579–1590, 2021.

[30] J. Wu e et al. Joint reconstruction of pet and mr images using a unified framework. *IEEE Transactions on Medical Imaging*, 32(4):699–710, 2013.

[31] S. Yamamoto, H. Watabe, Y. Kanai, e et al. Interference between pet and mri subsystems in a silicon-photomultiplier-based pet/mri system. *Physics in Medicine & Biology*, 56(13):4147, 2011.

Abstract

The technology of positron emission tomography combined with magnetic resonance image (PET/MRI) constitutes a comparatively novel imaging modality that combines PET's ability to trace metabolism with MRI's ability of tissue differentiation. This tool analyzes the structure and function of tissues and organs.

Although PET/MRI offers many significant advantages, its limitations must be considered. These scans may take longer than MRI and PET/CT due to the need to acquire detailed images from both modalities. This can increase the risk of movement during the exam, affecting image quality.

In addition to artifacts caused by patient movements, the hardware of both scanners interferes with each other, causing attenuation in the images. Furthermore, PET/MRI technology is expensive to acquire and operate. The high cost of the scanners can be a significant barrier, especially in health systems with limited resources.

This research uses prior information (PI) extracted from PET data, which was acquired simultaneously with MRI from Siemens ® PET-MR equipment, Biograph mMR. We have explored the fact that PET and MR images are acquired simultaneously to use information from PET modality to MRI and Compressive Sensing to enhance PET-MR image reconstruction.

This methodology exploits PET information to reduce the number of samples required to obtain the same MR image quality obtained with more measurements. In CS theory, this is equivalent to improving the quality of MR images for the same number of measurements.

The proposed method extracts information corresponding to the positions of non-null elements in the sparse representation of PET images, given that CS explores the sparse representation. This requires aligning the PET and MR images, as well as adjusting the spatial resolution to the same level, by nearest neighbor interpolation methods to reduce the size of the images and bilinear interpolation to increase the size of the images.

We tested the approach by varying the percentage of coefficients in the sparse representation considered as non-null element positions (and therefore used as a priori information) from 0 to 90 %, with 10 equally spaced values. We also varied the number of angles used from MRI from 10 to 160 angles, with 7 equally spaced values.

Image quality was evaluated quantitatively using signal-to-error-ratio (SER) and structural similarity index measure (SSIM). The opinions of radiologist specialists were not collected to sustain a qualitative analysis.

With a PI proportion of 10 %, the reconstructed images quality improves compared to those reconstructed without PI for all ranges of angles tested. Images reconstructed with 60 angles had an average SER of approximately 16dB and an average SSIM of roughly 0.82, while the images reconstructed with 10 % of PI had an average SER of 20dB and an average SSIM of approximately 0.89.

Based on the results obtained in this study, the proposed method demonstrates the potential to improve MRI image quality using PI from PET images extracted simultaneously from the same slice and spatial resolution. The use of PI from PET images for MRI reconstruction increased image quality even with a low number of measurements. With 35 angles, we obtained a SER of 20 dB. This approach can help to reduce the number of measurements required for MRI reconstruction in PET/MRI equipment.

For future work, we suggest the use of PI from MR image to reconstruct PET images. In addition, investigating this methodology for different trajectories and regions of the body can provide relevant information about its applicability. Another potential investigation is to use the k-space measurements extracted from the PET/MRI machine.

Keywords: PET/MRI, Compressive Sensing, Image Reconstruction, Prior Information

Contents

1 Introduction **1**

1.1 The Context of Medical Images 2

1.1.1 Magnetic Resonance Images 2

1.1.2 Positron Emission Tomography 3

1.1.3 PET-MR Scanners 3

1.2 Image Reconstruction 4

1.2.1 Compressive Sensing 5

1.2.2 Prior Information and Compressive Sensing 6

1.3 Research Problem 7

1.3.1 Related Work 8

1.4 Objectives 9

1.4.1 Main Objective 9

1.4.2 Specific Objectives 9

1.5 Project Scope 11

1.6 Structure of the Thesis 11

2 Magnetic Resonance and Positron Emission Tomography Devices **13**

2.1 Magnetic Resonance Images 14

2.1.1 Magnetic Resonance Image Device Principles 14

2.2 Positron Emission Tomography Images 22

2.2.1 Positron Emission Tomography Basic Principles 22

2.2.2 Limitations Inherent to Positron Emission Tomography 25

2.3 Positron Emission Tomography within a Magnetic Resonance Device . . 25

2.4 Changes in PET and MRI for PET/MRI fusion 26
2.4.1 Challenges in PET/MRI Integration 27

3 Image Reconstruction and Compressive Sensing 29

3.1 Signal Processing and Sampling 29
3.1.1 Fourier transform 32
3.1.2 Sampling 32
3.2 Compressive Sensing 34
3.3 PET-MR Image Reconstruction 36
3.3.1 Compressive Sensing Applied to PET/MRI 37
3.4 Research Problem 38
3.5 Related Work 39

4 PET-MR Imaging Proposed Method 41

4.1 Research Scope 42
4.2 Development Methodology 44
4.2.1 Extraction of k-space measurements from the MR images 45
4.2.2 Compressive sensing with pre-filtering applied to MRI images, without prior information from PET images 46
4.2.3 Extraction of prior information from PET images for reconstruction of MRI images 47
4.3 Experimental Procedures 47
4.4 Methods for Results Analysis 48

5 Results and Discussion 49

5.1 Dataset 51
5.2 Proposed Method Performance 51

6 Conclusion 57

References 59

List of Tables

4.1 Dataset studies description. 45

5.1 Diferent values of p for tests performed between the mean Signal-to-noise ratio (SER) for 100 images with 0 and 10 % of Prior Information (PI). . . 53

List of Figures

2.1 Ilustration of nucleus movment. The image illustrates the precession of a nuclear magnetic moment in the presence of a magnetic field (**B**). The nucleus, possessing a magnetic moment, experiences a torque when placed in the magnetic field. This torque causes the magnetic moment to precess around the direction of the main magnetic field. The frequency of this precession is known as the Larmor frequency. 15

2.2 Stages of Nuclear Magnetic Resonance (NMR) in a simplified representation. The figure describes the proton's spin behavior in different stages of the nuclear magnetic resonance process. Black circles represent the protons, and small arrows present the proton's spin directions. Figure A illustrates the protons spins behavior without the action of the Magnetic Resonance (MR) main magnetic field (B_0), the spins are precessing randomly, resulting in a zero net magnetization. Figure B represents the patient inside the MR scan. The protons are now in the presence of the main magnetic field (B_0), and the proton's spins are aligned to B_0, in parallel or anti-parallel direction, creating a net magnetization (M_z) along the direction of B_0. At this moment, M_z is at its maximum value. Figure C represents the spin behavior when the Radio Frequency (RF) pulses are applied perpendicular to B_0, with the Larmor Frequency, this pulse excites the nuclei, causing them to tip away from their alignment and precess around the RF pulse direction, at this moment the magnet moment is maximum at the RF pulse direction and 0 in B_0 direction. Figure D represents the spin's behavior once the RF pulses are withdrawn. The spins gradually return to their equilibrium state, aligning with the main magnetic field. This process is known as relaxation, occurring at different rates for different tissues. In Figure E, the spins have completely returned to their equilibrium state and are aligned with the main magnetic field B_0. 16

2.3 The image illustrates a simplified representation of a proton's behavior within the magnetic field (B_0). The proton, represented by a gray sphere, is subjected to torque due to the interaction of its intrinsic magnetic moment with the external magnetic field. This torque causes the proton's magnetic moment to precess around B_0 direction, the frequency of this precession is known as the Larmor Frequency. The dashed circle around the proton represents this movement. The straight arrows represent the B_0 direction. The smaller circular arrow on the proton indicates its intrinsic spin. . . . 17

2.4 Free Induction Decay (FID) signal in MRI. The graph visually represents the time-domain behavior of the nuclear magnetic resonance (NMR) signal in Magnetic Resonance Image (MRI). The blue sinusoidal component reflects the precession of the protons. At the same time, the red exponential decay shows the overall decay of the signal amplitude due to relaxation processes, at a rate called relaxation time (T_2). After applying the RF pulse, the protons are excited out of equilibrium and begin to precess around the RF pulse direction. This precession induces a time-varying magnetic field detected as an electrical signal in the receiver coil. The amplitude of this signal gradually decreases over time when the RF pulse is withdrawn. The graph was generated using Python programming language. 18

2.5 Longitudinal Relaxation (T_1) Curve. The graph illustrates the longitudinal magnetization (M_z) proton's behavior when the RF pulse is withdrawn. The blue curve illustrates the growth of longitudinal magnetization over time. After an RF pulse tips the magnetization away from the B_0 direction, the protons gradually realign with the B_0 field after the RF pulse is withdrawn. The rate at which this realignment occurs is characterized by the T_1 relaxation time. The red dot marks the point where the magnetization reaches approximately 63 % of its maximum value. The time corresponding to this point is the T_1 relaxation time. The graph was generated using Python programming language 19

3.1 Signal continuous in the time domain. The graph presents a continuous-time sinusoidal signal. The x-axis represents time, while the y-axis represents the wave's amplitude. The wave exhibits periodic behavior, repeating itself over a fixed interval. The graph was generated using the Python programming language. 31

3.2 Example of a discrete-time sinusoidal signal. The graph presents a discreet-time sinusoidal signal. This means that the signal is defined only at specific, discrete points in time instead of a continuous signal, which is defined for all points in time. The spacing between the discrete points on the time axis represents the sampling rate. 31

3.3 Sparse Signal. 34

4.1 Dataset Organization Structure. 44

5.1 Images extracted from the dataset. Figure A is an MR image; Figure B is the PET image from the same position, and Figure C is the two images fused and aligned to form a pair of PET/MRI. 51

5.2 The mean values of SER of 100 images for 7 different numbers of angles equally distributed between 10 and 160. For each number of angles, the experiment was reproduced for different proportions of PI, from 0 to 10 %. Where the images reconstructed with 10 % of PI had the best SER. . . . 52

5.3 The mean values of SSIM of 100 images for 7 different numbers of angles equally distribute between 10 and 160. For each number of angles, the experiment was reproduced for different proportions of PI, from 0 to 10 %. Where the images reconstructed with 10 % of PI had the best SSIM. . . . 52

5.6 Image reconstructed with 85 angles. Figure A was reconstructed without PI, and Figure B was reconstructed using 10 % of PI. 54

5.7 Images reconstructed with 10 % of PI for different angles. Figures A to F are the MR images reconstructed with the interval of 35 to 160 angles equally spaced. It is possible to notice that from Figure C to F the images are very similar. 55

5.8 Diferent scenarios comparison. Figures A, B, and C are images reconstructed with 10 angles with 0 %, 10 % and 90 % of PI. Figures D, E, and F are images reconstructed with 35 angles and 0 %, 10 %, and 90 % of PI. It is possible to observe an improvement in quality between Figures A and B, although the images still have low resolution; in Figure C, it is clear that there was a drop in image quality. Figures D, E, and F significantly improve resolution, with Figure E having greater visual quality. This supports the hypothesis that images with 10 % of PI present better results. . 55

List of Nomenclatures and Abbreviations

MRI Magnetic Resonance Image

MR Magnetic Resonance

PET Positron Emission Tomography

CS Compressive Sensing

PI Prior Information

PET-MR Positron Emission Tomography and Magnetic Resonance

PET/MRI Positron Emission Tomography and Magnetic Resonance Image

CMR Cardiac Magnetic Resonance

CT Computed Tomography

SPECT Single-photon Emission Computed Tomography

AD Alzheimer's disease

PET/CT Positron Emission Tomography and Computed Tomography

FID Free Induction Decay

RF Radio Frequency

PMT photo-multiplier

AB-AC Atlas-Based Attenuation Correction

CNNs Convolutional Neural Networks

fMRI Functional Magnetic Resonance Image

FDG Fluorodeoxyglucose

LOR Line of Response

TOF Time of Flight

FFT Fast Fourier Transform

FBP Filtered Back Projection

DCT Discrete Cosine Transform

DFT Discrete Fourier Transform

SER Signal-to-noise ratio

SSIM Structural Similarity Index Measure

LIT linear and time-invariant

OSEM Ordered Iterative Reconstruction

1 Introduction

Positron Emission Tomography and Magnetic Resonance Image (PET/MRI) scanners combine Positron Emission Tomography (PET) ability to trace metabolism with MRI ability for tissue differentiation [126]. This imaging modality is increasingly important in modern medicine because it provides detailed and complementary information about the anatomy and function of tissues and organs [9]. While PET is good for visualizing metabolic and physiological processes and identifying areas of high metabolic activity, such as tumors, MRI offers high anatomical resolution, allowing detailed visualization of the body's internal structures [191].

Although PET/MRI offers many significant advantages, its limitations must be considered. These scans may take longer than MRI and Positron Emission Tomography and Computed Tomography (PET/CT) due to the need to acquire detailed images from both modalities [135].

The increased acquisition times can lead to higher risks or levels of involuntary patient movements, thus leading to more movement artifacts [3]. In addition to artifacts originated by patient movements, the hardware of both scanners causes interference with each other causing attenuation in the images [107, 192].

Furthermore, PET/MRI technology is expensive in acquisition and operation [49, 57]. The high cost of the scanners can be a significant barrier, especially in health systems with limited resources.

Due to cost and complexity, the availability of PET/MRI systems is limited. This may restrict access for patients in rural or less developed areas. According to research conducted in 2015 there was 110 PET/MRI devices spread across the word, with 85 % of them installed in Europe and North America [53].

This research proposes and develops a method for image reconstruction in PET/MRI that explores cross prior information extracted from one of the images to improve imaging in the other modality. We argue that this method may reduce the effects of PET/MRI attenuation, and also reduce the number of measurements required to attain a certain image objective quality. For this we used PI of PET images to reconstruct MR images with Compressive Sensing (CS) and pre-filtering.

This chapter presents the importance and application of MRI and PET and how PET/MRI allies the most substantial aspects of both modalities. Then, it discusses image reconstruction, CS, pre-filtering, and PI. After this short explanation, it presents the goal and aims of this research and the text structure.

1.1 The Context of Medical Images

Medical imaging is a significant field for diagnostics and therapy. Its history began in 1895 with the X-ray discovery by Wilhelm Conrad Roentgen [19]. Through his studies, Roentgen discovered X-rays while working with Crookes tubes. He observed that these rays could pass through opaque materials and create images of internal structures on photographic plates [149].

In 1972, Godfrey Hounsfield and Allan Cormack developed the method of Computed Tomography (CT) by X-rays [75]; due to this important discovery, they won the Nobel Prize in Medicine, in 1979. Their method used X-rays to create detailed cross-sectional images of the body, making it possible to acquire images from its internal structures.

A year later, Paul Lauterbur and Peter Mansfield developed the basis of MRI [99], and, for that, they won the Nobel Prize in Medicine. Today, several medical image modalities coexist, due to each one's particularities and advantages [1].The main ones are: CT, MRI, PET, Single-photon Emission Computed Tomography (SPECT), ultrasound imaging, termography imaging, X-ray imaging, and optical imaging. In this research, I will focus on MRI and PET, acquired simultaneously by the same equipment.

1.1.1 Magnetic Resonance Images

Due to its physical principles, MRI has good resolution and tissue differentiation capacity. A study [168] showed that it is possible to detect the reduction of connectivity between the pre-frontal cortex and other parts of the brain through MRI data, indicating improvements in early diagnosis of Parkinson's disease.

Another aspect of this modality is that it is non-invasive. For instance, it is possible to predict pulmonary capillary wedge pressure used to indicate raised left ventricular filling pressure via Cardiac Magnetic Resonance (CMR) method. These results may help to detect heart failure and patients with a risk of death [59].

MR can also have potential applications for cancer treatment. As indicated in [170], where the hyperthermia produced by the magnetic field associated with a nanoparticle, can decrease the size of glioma cells in brain tumors. A similar methodology was investigated in [167].

Machine learning techniques are also being employed to MRI for automatic diagnosis. A logistic regression and neural network method were applied to the images to classify brain tumors into several categories, like glioma and meningioma [102]. Another study used MRI machine learning techniques for brain tumor diagnosis and treatment [71].

1.1.2 Positron Emission Tomography

Although MRI is a powerful tool for functional, molecular, and anatomic investigation, it has limitations for metabolic analysis, due to the acquisition times that reduce the maximum time resolution for a given spatial resolution [67]. For metabolic analysis, PET constitutes one of the best available imaging modalities [32]. PET evaluates lesions metabolism identifying molecular changes before CT and MRI.

However, PET images may be difficult to interpret. PET images typically have lower spatial resolution than CT and MRI, and variations in area activation due to metabolic differences can be comparatively complex to locate spatially for anatomical structures [15]. Thus, the use of CT or MRI to help create a map of the body is needed.

Images of PET can be used to quantify the degree of an inflammation [152], to understand the pathophysiology of diseases such as Parkinson's [130], and to classify Alzheimer's disease (AD) [155]. Research done with deep learning, using PET images, was able to diagnose AD early [144]. Another potential applications were described by [159], where PET images were used to evaluate the relationship between physical activity, sleep quality, and cognitive function.

Whereas PET/CT has been developed for combining the spatial resolution of CT with the metabolic analysis potential of PET, the combined analysis of different anatomical structures with the provided metabolic information is still limited [164]. Besides that, CT and PET images are not acquired simultaneously, this can cause problems with noises caused by organ motion and patient breathing capabilities [13].

On the other hand, MRI generates detailed anatomical images but does not provide information about the metabolic or molecular function of tissues [68]. This could cause difficulty detecting diseases with subtle metabolic changes, limiting its usefulness in some cases. Due to this limitation of PET/CT equipment, the PET/MRI devices were proposed and developed as an alternative for anatomical analysis combined with metabolic analysis.

1.1.3 PET-MR Scanners

PET/MRI has established itself as a useful technique in diagnosing and following various diseases [20, 52, 109, 39]. It offers high-quality functional and anatomical images

with low levels of ionizing radiation [125, 158].

The combination of PET and MRI overcomes the limited spatial resolution of PET,allowing for a better visualization of both anatomical and functional details. PET/MRI provides detailed anatomical images from MRI and functional images from PET in a single exam, eliminating the need for additional exams [178].

PET/MRI uses radioisotopes in smaller quantities than traditional PET [158], resulting in a significantly lower radiation dose for the patient. The combination of anatomical and functional information from PET/MRI allows for better disease characterization, facilitating diagnosis, staging, and treatment monitoring.

This modality may improve the diagnostic in the epileptogenic zone of MRI-negative cases of epilepsy and improve surgical outcomes [66]. It could also improve brain malignancy perception, preventing unnecessary invasive procedures and helping distinguish between tumor progression and therapy-related imaging alteration [20].

1.2 Image Reconstruction

The importance of imaging exams is undeniable [97]; for this matter, improving and optimizing imaging techniques is crucial to enhance image quality and patient safety. Therefore, reconstruction techniques are a vital part of the continuous advancement of medical diagnostics, treatment planning, and modeling.

Image reconstruction is a process that converts the actual scene into its image representation [200], based on measurements of such scene by specific sensors. For instance, imagine you are looking at a garden full of lilies. The flowers you see reflect light that your eyes capture. Each color has a different wavelength that is recognized by your corneas. The result signals are transmitted to your brain, and is converted into an image. This is a reconstruction process.

Ideally, all the measurements needed to reconstruct an image with theoretically perfect accuracy should be considered. But this is not the case, especially for medical images. The acquisition time is long, and the patient cannot stand still for too long, this can cause artifacts. Due to data under-sampling, linear reconstruction techniques can lead to aliasing artifacts according to the Nyquist criterion [132]. For this reason, one of the challenges in the medical imaging field is to reduce the number of signal samples without losing image quality.

1.2.1 Compressive Sensing

Reconstruction techniques from incomplete samples from a Fourier representation are essential for improving several scanning technologies [136]. A lot of effort is driven to find methods to restore the image with a limited number of samples [34, 69, 90].

Unlike traditional methods that require the acquisition of a complete data set, CS allows the rebuilding of high-quality images with a significantly smaller number of measurements.

The theory assumes that most data acquired in the measurement process is redundant and exploits the property that images often have high sparsity in a transformed domain, such as the transformed wave domain. This sparsity means that the image can be represented with relatively few non-zero coefficients. By exploiting this sparsity, CS allows for image reconstruction from an undersampled set of data [118].

This theory is beneficial where the information is limited, in which acquiring different measurements is considered expensive, in terms of energy comsumption, sensors, time, or a combination of these factors, but in which some knowledge about the signals' efficient representations may allow us to represent the information in terms of fewer, well-acquired measurements. CS method is already used for MRI reconstruction [204, 121, 79, 61]. And it has been applied for PET-MR reconstructions as well [93].

With CS, it is possible to recover the image from fewer measurements, saving acquisition time. It depends on sparsity, which is determined from prior knowledge of the image structure when many of its coefficients are zero or near zero in a transform domain, such as a Discrete Cosine Transform (DCT) or wavelet domain. Several studies used the CS techniques in medical image compression, proving its efficiency [7].

Lately, CS has made findings from both the engineering applications perspectives and theoretical perspectives [187]. Distinct from other compressing techniques, this method has an advantage in some of the slower sampling circumstances, such as magnetic resonance imaging MRI and computed tomography CT, where a slow sampling rate is a significant drawback [145].

In both cases, we want to take fewer measures. In the first case, to reduce time and, consequently, the risk of movement artifacts, in addition to exam costs and difficulties associated with patient comfort. In the second case, to reduce the radiation the patient is exposed to. In both cases, CS makes it possible to use fewer measurements and obtain images of the same quality as classical reconstruction techniques (spectral interpolation or NUFT with interpolation in the MR case and filtered back-projection in the CT case). In CS theory, this is equivalent to having better images when using the same measurements [115].

In PET/MRI, CS can improve image quality and reduce acquisition time in myocardial perfusion studies, allowing for a more accurate assessment of cardiac function according to [189].

It can also aid in detecting and characterizing tumors, providing more accurate functional and anatomical information. It can also be applied in functional neuroimaging studies, such as Functional Magnetic Resonance Image (fMRI), to improve image spatial and temporal resolution [108].

1.2.2 Prior Information and Compressive Sensing

After the initial developments of CS, subsequent theoretical and empirical advances have led to even further reductions of the number of measurements required to attain an established image quality. One of the most important theoretical advances is the use of PI. In some scenarios, a previously acquired image may be available to provide information useful for reconstructing a new image [122].

For example, consider a set of slices in a three-dimensional structure. Suppose part of the structure is reconstructed before another part. In that case, slices from the previous reconstruction can provide information that aids the continued reconstruction process because the rate of change between slices is limited. Therefore, the percentage of locations of known-zero elements in the sparse representation is expected not to change. Also, in a temporal sequence of images, for example, in a PET sequence, a frame has common elements for a previous frame. In this case, the temporal redundancy can also be explored. In both these contexts, CS reconstructions have benefited from using prior information, defined as information from a previous set of signals [118] or data (in our context, images) that is statistically expected to have common elements that can aid the further algorithm's stages.

Incorporating a priori information in image reconstruction with CS can significantly improve the results, leading to images with higher spatial resolution, lower noise, and better fidelity to the original scene [180, 116, 81].

This information can come from various sources, such as anatomy, texture, or expected patterns in the image, low-resolution or noisy images of the same scene, mathematical models that describe the image acquisition process, or the statistical characteristics of the data.

The use of PI can help reduce noise, preserve fine details, and correct artifacts, resulting in more accurate images with better visual quality. By exploiting the correlations present in a priori information, CS can reconstruct images with spatial resolution higher than possible with traditional methods [169].

It can also allow the reconstruction of high-quality images from an even more undersampled dataset [117], reducing the acquisition time and radiation dose in cases of imaging with PET/MRI and in addition to making the reconstruction process more robust to the presence of noise and interference in the raw data, leading to more reliable results [128].

The use of CS with PI can be used to significantly reduce the radiation dose in CT scans, minimizing the risks to the patient [48]. This method can help accelerate imaging acquisition in MR, allowing faster and more comfortable studies for patients [104].

In PET/MRI, PI can be extracted from various sources, each providing different knowledge to complement the reconstruction process. For example, 3D anatomical models (such as brain atlases or bone models), low-resolution or noisy images of the same scene (CT scans or MRIs), intrinsic properties of raw data (such as the spatial distribution of activity in the PET image), or even physiological models that describe the distribution of metabolic activity or blood flow in the human body [165].

1.3 Research Problem

Although PET/MRI is a promising advanced technology for medical imaging, it is an expansive resource, and its physical structure causes image attenuation due to the main magnetic field and PET compatibility [17, 129, 147].

The conventional PET uses photomultiplier tubes photo-multiplier (PMT), but when attached to a MRI device, they suffer interference by the high magnetic field [137]. Improving and optimizing imaging techniques for Positron Emission Tomography and Magnetic Resonance (PET-MR) is crucial to enhance image quality and accessibility.

Gamma-ray attenuation also affects the clarity and accuracy of the images. This attenuation is influenced by the patient's tissue density, position in the scanner, and even the material the scanner coils are made of. All these factors can distort the image and make it hard to measure how much radiotracer is absorbed by different tissues [182].

Even so, investigating methods to overcome these challenges contributes to generating new knowledge about the human body, diseases, and their treatment responses. This leads to groundbreaking scientific discoveries, the development of new drugs and therapies, and the improvement of patients' quality of life.

To overcome the attenuation problem, a technique called Atlas-Based Attenuation Correction (AB-AC) uses an atlas of CT or MRI to estimate the distribution of attenuation in the patient's body [96]. Machine learning techniques are being explored as a solution [5, 29, 95, 101, 199]. Algorithms based on Convolutional Neural Networks (CNNs)

are trained on large PET/MRI and CT image datasets, learning to identify complex attenuation patterns and estimate the spatial distribution of attenuation with high accuracy. Solutions with computational physics are investigated as well. Computer simulations of gamma-ray transport physics provide a robust basis for attenuation correction in PET/MRI [96].

In [16], the reconstruction of PET and MRI images are performed in a single iterative process. The results show that integrating PET and MRI information allows for identifying and eliminating image artifacts caused by inconsistent attenuation, improving visual quality and reliability.

This work seeks to explore the fact that the images are simultaneously acquired to use PI of PET images and CS to reconstruct MR images and improve image quality. Previews work used PI information from one modality to another from a generalized joint sparsity regularization [112], as a joint PET/MRI patch-based dictionary modeled as a Markov random field for Bayesian reconstruction [166], with blurry random data from PET under-determined Fourier data with Gaussian noise from MRI [50]. But did not use PI from the same slice position from one modality to another with CS and pre-filtering.

This type of PI is expected to benefit the reconstruction because they are acquired from the same frame and slice. This can result in better images for the same number of measurements from PET and MRI used in PET/MRI acquisitions. If the hypothesis is sustained, this may compensate the noise caused by the interference between the two technologies.

There are technical problems to be solved that require investigation: the images are in different resolutions, and they may not be perfectly aligned despite being simultaneous. However, they are treatable.

1.3.1 Related Work

Even though CS is already commonly used in medical image reconstruction, especially in MRI, we found few studies applied to PET/MRI case [56, 112]. On the other hand, the fact that the images are simultaneously acquired was explored to extract information from one to another in several cases [166, 50].

The study in [113] provides evidence that a set of MRI data can improve PET image quality in terms of Signal-to-noise ratio (SER) and Structural Similarity Index Measure (SSIM). It also proposes a method of MRI denoising using CS. However, we did not find a study where PI of PET is used with CS to reconstruct MR images from PET-MR devices.

The use of PI from one modality to the other has already been proven a successful

approach to overcome PET/MRI attenuation challenges [58]. It is also known that using CS and PI can reduce the number of samples required in the reconstruction process [163]. Based on these findings, and the fact that PET/MRI suffers from attenuation caused by PET hardware on the main magnetic field of the MR scanner in addition to the noise caused by patient motion. Based on these findings, and the fact that PET/MRI suffers from attenuation caused by PET hardware on the main magnetic field of the MR scanner, the relevance of extending the use of prior information in CS to this type of technology becomes clear.

1.4 Objectives

This research addresses the use of PI extracted from PET data, acquired simultaneously with MRI from Siemens PET-MR equipment, Biograph mMR. I seek to explore the fact that PET and MR images are acquired simultaneously to use information from PET modality to MRI and CS to enhance PET-MR image reconstruction.

Note that the studies in [118, 58] had already successfully similar approaches in CT and functional MRI.

1.4.1 Main Objective

The main goal of this study is to develop and evaluate imaging methods using Prior Cross-Information from PET images for MRI to improve the objective quality of the images. With this objective, I aim to respond to the following research question: "What is the Signal-to-noise ratio (SER) and Structural Similarity Index Measure (SSIM) obtained when applied PI from PET images combined with CS algorithms to reconstruct MR images?".

1.4.2 Specific Objectives

To achieve this research's main goal, I decomposed it into small specific objects, that allowed me to answer objectively secondary research questions. I connected some of the specific objectives to research questions, in the case of very direct related cases.

- Develop a program for alignment and resolution adjustment of PET and MRI image pairs, since in the set of images provided by Siemens (described in 4), there was no direct alignment information, and the resolutions are different (as expected for these image pairs). Alignment is necessary for the extraction and use of information a priori.

- Develop a program for extracting information from PET images already aligned with MRI images, for use in CS. The extracted information must occur in the sparse representation adopted for the reconstruction by CS.

- Develop a program for reconstruction of MRI images using information extracted from PET images and based on compressive sensing.

- The use of PI information of PET images in CS algorithms can reduce the number of measurements needed to reconstruct MRI by how much?

  Observe if the use of PI of PET images in CS algorithms can reduce the number of measurements required in MRI reconstruction process.

- How many measurements are necessary to maintain MRI quality using PI information from PET images?

  Observe the minimum number of measurements necessary to maintain MRI quality using PI information from PET images.

- How many measurements are necessary to improve MRI quality using PI information from PET images?

  Observe the minimum number of measurements necessary to improve MRI quality using PI information from PET images.

- What PI percentual is necessary to maintain MRI quality in an interval of 7 angles equally spaced from 10 to 160?

  Observe the minimum PI percentage necessary to maintain MRI quality in an interval of 7 angles equally spaced from 10 to 160.

- What PI percentual is necessary to improve MRI quality in an interval of 7 angles equally spaced from 10 to 160?

  Observe the minimum PI percentage necessary to improve MRI quality in an interval of 7 angles equally spaced from 10 to 160.

- What PI percentual is necessary to reduce MRI quality in an interval of 7 angles equally spaced from 10 to 160?

  Observe the minimum PI percentage necessary to reduce MRI quality in an interval of 7 angles equally spaced from 10 to 160.

- What is the relation between PI percentage and the number of measurements?

  Observe the relation between PI percentage and the number of measurements.

- What are the maximum SER and SSIM values obtained with the proposed method?

  Observe the maximum SER and SSIM values obtained with the proposed method.

- What is confidence in the experiment's results?

  Perform a statistical analysis of the results.

1.5 Project Scope

In this project, I will investigate the effect of the use of PET PI to reconstruct MRI with CS algorithms, for PET and MR images acquired simultaneously from the Simens Biograph mMR PET/MRI device.

The quality of the images will be evaluated from a quantitative point of view. I will use SER and SSIM metrics to assess the quality of the images. The qualitative evaluation requires the participation of radiologists and other health professionals, and is a topic for a future study, if the objective metrics indicate the expected improvement.

The data used for this research was extracted from the Biograph mMR. Siemens gave access to the images in DICOM format for academic use. Although the study cases were picked up randomly, the pairs of images used in this investigation were not chosen randomly. This scenario is justified by the lack of study examples with pairs of PET and MR images.

1.6 Structure of the Thesis

The remainder of the dissertation is organized in the following manner: two chapters on the theoretical foundation, a chapter on results and discussions, and, finally, the conclusion. The next two chapters of this dissertation are the theoretical foundation on medical images and image reconstruction. First I explain MR and PET fundamentals and the image formation process. This is important to comprehend how the images are formed and why it is essential to search for reconstruction methods. Then, describe the main changes in PET to be integrated into the MRI scanner and the attenuation problem with PET/MRI.

After this chapter, I explain image reconstruction and the CS theory and how the method is applied in the medical image scenario. At the end of this chapter, I explain this research's aims and the theory that supports this study's hypothesis.

Later, the third chapter, discusses the pre-filtering and PI extraction method applied in this work, how the experiments were designed, and under what conditions they were executed. The next chapter contain the results and discussion. Lastly, I describe the

conclusion of this research.

2 Magnetic Resonance and Positron Emission Tomography Devices

Images represent an object or a pattern. They are measurements taken from a scene. For instance, when an artist paints or draws a portrait, that Picture represents the measures of the light amplitude and wavelength reflected by the object and captured by the viewer's eye [24].

This chapter will describe how MR and PET images are acquired. Then, I will discuss PET-MR images and what changes are necessary to couple a PET machine to a MR scanner. In Chapter 3, I will explain image reconstruction, CS, PI, and pre-filtering.

Medical imaging is a field that employs various technologies to produce images of the inside of the human body for diagnostic purposes. These images provide doctors with valuable information about the anatomy, physiology, and function of organs and tissues, helping them diagnose diseases, plan treatments, and monitor therapeutic responses [4].

There are several types of images, each captured by a different device. In radiography, X-rays pass through the body to varying degrees according to the density of the tissues. Bones, being denser, block more radiation, while soft tissues allow more radiation to pass through [161]. X-rays usually are employed to diagnose fractured bones, pneumonia, bone tumors, and lung diseases [10].

Ultrasounds employ high-frequency sound waves emitted by a transducer and reflected by body tissues. The time it takes for the waves to return to the transducer is used to generate images in real-time, allowing visualization of the anatomy and movement of internal organs [31]. They help evaluate organs and soft tissues, such as the liver, kidneys, uterus, and ovaries [2].

Another modality that uses X-rays is the CT. It combines X-rays and computers to create cross-sectional (sliced) body images. The patient lies on a table that moves through a gantry, which emits X-rays at different angles. The images are reconstructed by a computer, generating detailed images [156]. These images are used to diagnose various diseases, such as tumors, heart disease, stroke, lung disease, and bone problems [76].

This work will focus on MRI and PET. The first one uses a strong magnetic field

and radio waves to create detailed images of organs [173]. The second uses radioisotopes injected into the patient's body, that accumulate in areas with high metabolism, such as tumors or areas of inflammation [12]. Knowing how these images are acquired is necessary to understand the reconstruction process and the proposed method.

2.1 Magnetic Resonance Images

Unlike other imaging techniques, such as radiography and CT, MRI does not use ionizing radiation, this makes it a safer option for children or pregnant women [88]. The modality provides high-resolution and contrast images, allowing the visualization of anatomical details that are not visible with other techniques. This is crucial for diagnosing complex diseases such as tumors, neurological diseases, and musculoskeletal problems [205].

They also can generate images in different planes (axial, coronal, and sagittal) that allow a complete three-dimensional assessment of the patient's anatomy [33]. This is important for planning medical procedures and evaluating disease progression. MRI's high resolution and contrast allow for diseases early diagnosis [78].

Phase-contrast MRI uses the MR signal to measure and visualize the speed of moving protons within the body. This technique can measure valve function and blood flow through heart valves, assess cerebrospinal fluid flow, and elastography [194].

In [8], diffusion MRI is used for exploring the brain's microstructure and the tiny details of its tissue. It explains how scientists are developing models to translate the MRI signal from a specific area into information about the microscopic properties of that tissue. This can help health professionals rely on biopsies for detailed tissue structure information.

2.1.1 Magnetic Resonance Image Device Principles

The MR scanner uses a measurement technique to quantify particles through an atom attribute called angular momentum. Nuclei with this property rotate at a constant velocity around the rotation perpendicular axis, as shown in 2.1. This movement generates a magnetic field called magnetic momentum [22].

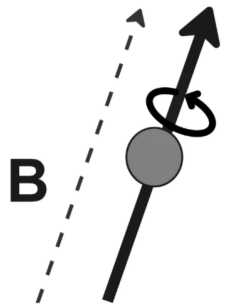

Figure 2.1. Ilustration of nucleus movment. The image illustrates the precession of a nuclear magnetic moment in the presence of a magnetic field (**B**). The nucleus, possessing a magnetic moment, experiences a torque when placed in the magnetic field. This torque causes the magnetic moment to precess around the direction of the main magnetic field. The frequency of this precession is known as the Larmor frequency.

Each nucleus has its quantized spin quantum number, determining the element's magnetic characteristics. There are limited ways a spin can rotate, which is called spin state. Each state has a magnetic moment proportional to the rotation mode [42].

Due to the abundance of hydrogen in nature and biological tissues, resonance imaging systems typically use its atoms as a reference in the measurement process. Outside the influence of an external magnetic field, the spin states have the same energy and different alignment as illustrated in Figure 2.2. When exposed to the main field of the MRI machine (B_0), these spins come into alignment [22] as shown in Figure 2.2.

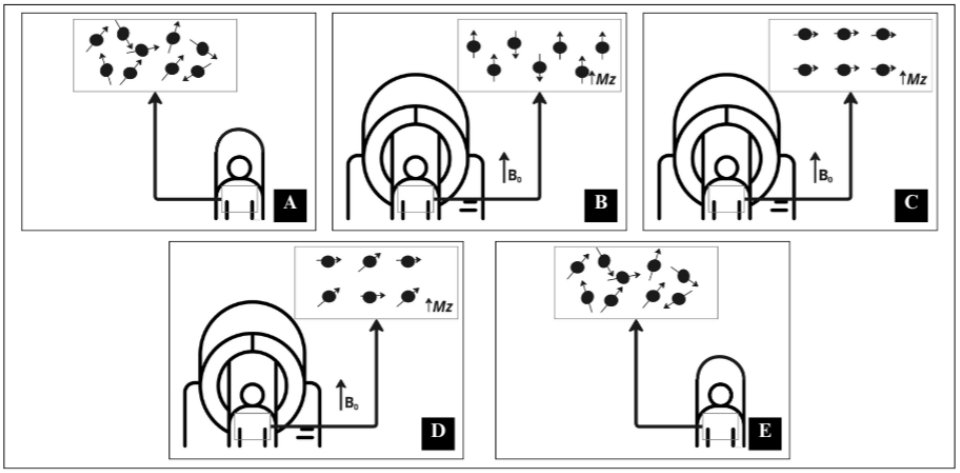

Figure 2.2. Stages of Nuclear Magnetic Resonance (NMR) in a simplified representation. The figure describes the proton's spin behavior in different stages of the nuclear magnetic resonance process. Black circles represent the protons, and small arrows present the proton's spin directions. Figure A illustrates the protons spins behavior without the action of the MR main magnetic field (B_0), the spins are precessing randomly, resulting in a zero net magnetization. Figure B represents the patient inside the MR scan. The protons are now in the presence of the main magnetic field (B_0), and the proton's spins are aligned to B_0, in parallel or anti-parallel direction, creating a net magnetization (M_z) along the direction of B_0. At this moment, M_z is at its maximum value. Figure C represents the spin behavior when the RF pulses are applied perpendicular to B_0, with the Larmor Frequency, this pulse excites the nuclei, causing them to tip away from their alignment and precess around the RF pulse direction, at this moment the magnet moment is maximum at the RF pulse direction and 0 in B_0 direction. Figure D represents the spin's behavior once the RF pulses are withdrawn. The spins gradually return to their equilibrium state, aligning with the main magnetic field. This process is known as relaxation, occurring at different rates for different tissues. In Figure E, the spins have completely returned to their equilibrium state and are aligned with the main magnetic field B_0.

At this point, the spins adopt two possible orientations: anti-parallel or parallel. Most atoms align to the state parallel to the magnetic field because it is the least energetic state. Due to the intense value of B_0

$$\vec{B_0} = B_0\vec{k}, \tag{2.1}$$

the spins oscillate randomly, around themselves and the magnetization axis at a frequency called the Larmor frequency, as shown in Figure 2.3, given by Equation 2.2

$$F = \gamma\frac{B_0}{2\pi} \tag{2.2}$$

where γ is the nucleus gyromagnetic radius [174, 25]. The gyromagnetic ratio of hydrogen is 42.58 MHz/T [74].

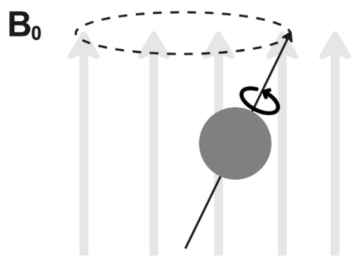

Figure 2.3. The image illustrates a simplified representation of a proton's behavior within the magnetic field (B_0). The proton, represented by a gray sphere, is subjected to torque due to the interaction of its intrinsic magnetic moment with the external magnetic field. This torque causes the proton's magnetic moment to precess around B_0 direction, the frequency of this precession is known as the Larmor Frequency. The dashed circle around the proton represents this movement. The straight arrows represent the B_0 direction. The smaller circular arrow on the proton indicates its intrinsic spin.

The net magnetic moment (M) is the sum of the magnetic moments of each spin contained in the analyzed tissue and is given by the Bloch Equation in Equation 2.3

$$\frac{d\vec{M}}{dt} = \gamma\vec{M} \times \vec{B} - \frac{M_x\vec{i} + M_y\vec{j}}{T_2} - \frac{(M_z - M_0)\vec{k}}{T_1} \tag{2.3}$$

where M_0 is the is the magnetic momentum of $Z-$axis in equilibrium in the presence of the magnetic field component B_0, T_1 and T_2 are the so-called longitudinal and transversal relaxation times. When the patient is exposed to B_0, the magnetic moment in the direction of the magnetic field (M_z) is maximal, and in the perpendicular directions (M_x) and (M_y), it is null [42].

2.1.1.1 Relaxation

When a RF pulse is emitted at the same oscillation frequency as the spins, there is a change in the energetic state of the hydrogen protons, which move to the most energetic state, the anti-parallel state. In other words, the protons align in the negative direction of the Z-axis [174]. This phenomenon is modeled by Equation 2.4

$$\vec{B_1}(t) = B_1^a \cos(\omega_f + \phi)\vec{i} + B_1^a \sin(\omega_f + \phi)\vec{j} \tag{2.4}$$

where B_1^a is the main characteristic of B_1, the envelop function, ω_f, is nearly the Larmor Frequency, and ϕ is the initial phase angle.

At this point, the oscillation movement is perpendicular to the Z-axis in the XY-plane, oscillating in phase with its maximum amplitude. After the pulse is emitted, the protons return to their equilibrium position, and the particles return to oscillation out of

phase around the Z axis; this process is called relaxation [103].

This change in the magnetic field induces an electric current in a coil. This signal is called Free Induction Decay (FID), and, as the protons return to their equilibrium state, the signal is reduced to a constant of time called relaxation time or transverse relaxation time (T_2) [111]. Figure 2.4 illustrates this process.

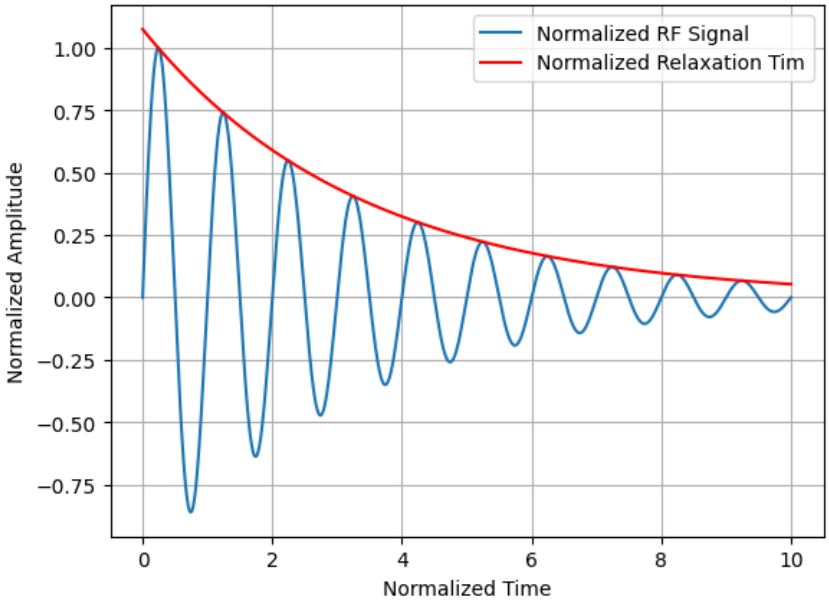

Figure 2.4. Free Induction Decay (FID) signal in MRI. The graph visually represents the time-domain behavior of the nuclear magnetic resonance (NMR) signal in MRI. The blue sinusoidal component reflects the precession of the protons. At the same time, the red exponential decay shows the overall decay of the signal amplitude due to relaxation processes, at a rate called relaxation time (T_2). After applying the RF pulse, the protons are excited out of equilibrium and begin to precess around the RF pulse direction. This precession induces a time-varying magnetic field detected as an electrical signal in the receiver coil. The amplitude of this signal gradually decreases over time when the RF pulse is withdrawn. The graph was generated using Python programming language.

There are two independent relaxation times: transverse and longitudinal. The transverse relaxation process has already been described. Longitudinal relaxation (T_1) is the time for the tissue to recover 63 % of its original longitudinal magnetization (M_z). This process generates a magnetic moment in the Z direction and grows exponentially [103], as shown in Figure 2.5. Equation 2.5 describe this phenomenon

$$M(\tau) = M_0(1 - e^{-\frac{\tau}{T_1}}) \tag{2.5}$$

where $M(t)$ is the magnetic moment in the Z direction.

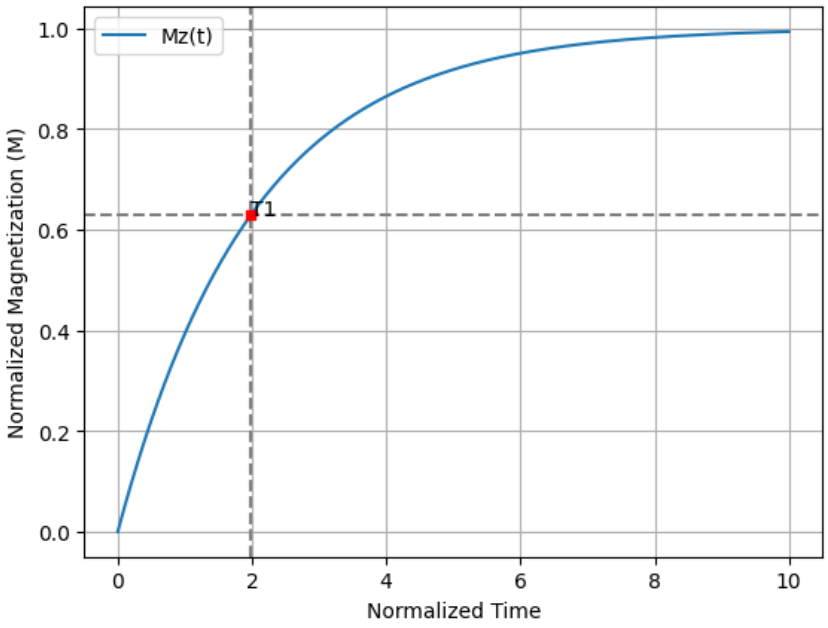

Figure 2.5. Longitudinal Relaxation (T_1) Curve. The graph illustrates the longitudinal magnetization (M_z) proton's behavior when the RF pulse is withdrawn. The blue curve illustrates the growth of longitudinal magnetization over time. After an RF pulse tips the magnetization away from the B_0 direction, the protons gradually realign with the B_0 field after the RF pulse is withdrawn. The rate at which this realignment occurs is characterized by the T_1 relaxation time. The red dot marks the point where the magnetization reaches approximately 63 % of its maximum value. The time corresponding to this point is the T_1 relaxation time. The graph was generated using Python programming language

Tissues with high water content, such as muscle and brain, have longer T_1 relaxation times, while tissues with low water content, such as bone and fat, have shorter T_1 relaxation times.

Theoretically, all protons are exposed to the same field, B_0, presenting the same frequency, FID. The varying magnetic field leads to a spectrum of decay frequencies. Therefore, it is easier to analyze these components in the frequency domain. The Fourier does this conversion transform. Three elements are essential for image formation: signal magnitude, frequency, and phase [42].

To generate the image slice, the machine generates a magnetic gradient called the slice selection gradient (G_{ss}); this gradient will cause the excitation of only one group of spins in a given region, depending on the frequency. The direction in which the gradient is applied informs the orientation of the slice. At the same time, the amplitude combined with the properties of the radiofrequency pulses provide information about the position and width of the slice [111].

The Transverse Relaxation (T_2) represents the time for protons to lose their transverse magnetization (perpendicular to the B_0). Tissues with local magnetic homogeneity, such

as muscle and liver, have longer T_2 relaxation times, while tissues with local magnetic heterogeneity, such as bone and fat, have shorter T_2 relaxation times [23].

The differences in T_1 and T_2 relaxation times between tissues generate contrast in MR images. For instance, tumors generally have different T_1 and T_2 relaxation times than surrounding healthy tissues, allowing their detection and characterization [190].

2.1.1.2 Radiofrequency Pulses

RF pulses in MRI consists of electromagnetic waves with specific frequencies (Larmor Frequency), carefully tuned to resonate with the precession frequency of protons present in biological tissues. This resonance occurs when the frequency of the RF pulse coincides with the frequency of proton rotation around the main magnetic field (B_0) of the MRI [111].

The protons absorb energy by applying a pulse at the resonant frequency, causing them to deviate from their state of alignment with the B_0 magnetic field and "spin" around the field axis. This rotation, known as precession, generates a detectable RF signal[103].

The pulse duration T_1 and excitation angle determine the amount of energy transferred to the protons and the magnitude of the signal. A shorter T_1 excites more protons but generates a weaker signal and lower contrast between tissues. On the other hand, a longer T_1 excites fewer protons but generates a stronger signal and greater contrast between tissues [23].

More protons are excited with a larger excitation angle but generate images with a lower SER. With a smaller excitation angle, fewer protons are excited but create images with higher SER. Several types of RF pulses are used in MRI: rectangular, Gaussian, high-power radiofrequency pulse, and low-power radiofrequency pulses. The pulses also differ by the modulation. That can be amplitude, phase, and frequency [148].

2.1.1.3 Spatial Encoding

The imaging of standard MRI machines is based on gradients, that generate wave modulations in the transverse magnetic field ($M(r)$). This field oscillates in the direction of the main magnetic field and creates radiofrequency fields detected in the receiving coils. Ideally, the signal received in the coil is given by Equation 2.6 [142]

$$d_k = \int M(r) e^{-jk_k r} dr \tag{2.6}$$

Where d_k is the signal received in the coil. Frequency excitation, denoted by G_{ss}, is employed to locate the region of impulse application. The direction of the gradient determines the orientation of the slice, and its amplitude, combined with other characteristics of the RF pulse, indicates the position and thickness of the slice. A frequency-selective RF pulse has two components: a center frequency and a frequency band.

When the RF pulse is subjected to the gradient of shear selection, only a portion of the tissue will reach the resonance conditions and absorb the energy of the RF signal. The central frequency indicates the excited location in the presence of the gradient. On the other hand, the width of the slice is given by the amplitude of the gradient and the bandwidth of the frequencies, as shown in Equation 2.7

$$\Delta\omega_{ss} = \gamma(G_{ss} \times L) \tag{2.7}$$

Where $\Delta\omega_{ss}$ is the bandwidth of the frequencies, and L is the width of the slice. When a linear transverse gradient is applied after excitation, the distribution of the Larmor frequency along the transverse axis will be linear. This will result in a variation of the magnetization phase. After removing the field, the phase will remain proportional to the transverse axis.

When a constant gradient field is applied to the sample, the vibration frequency will change linearly according to the spatial location. If a signal reading is taken while the gradient is on, different places in space will have different frequencies.

At the end of this process, the phase and frequency variations will "tag" each point in the cut space with a phase and a frequency. The integral of this pattern is the Fourier transform. The signal measured during this procedure produces a line in the frequency domain called the k-space. The inverse transform of this matrix is applied to obtain the image.

2.1.1.4 MRI in the clinical scenario

MRI produces detailed and high-resolution images. This enhanced resolution enables the visualization of intricate anatomical structures, including fine details and subtle abnormalities that might go undetected using other techniques [92].

MRI differentiates between soft tissues, such as muscles, tendons, ligaments, and internal organs. Recent studies have highlighted its ability to differentiate lesions in bone tissue [83]. The superior contrast is attributed to its ability to detect the magnetic properties of hydrogen, abundant in soft tissues. This contrast distinction allows for precisely identifying lesions, tumors, and other abnormalities within soft tissues [201].

The imaging modality has become an essential tool in medical diagnosis, providing detailed and accurate images of various human body organs and tissues. However, like any diagnostic method, MRI has limitations that must be considered to ensure the correct interpretation of results and patient safety. Although MRI's spatial resolution is high, it can still be limited in some applications, making it challenging to visualize microscopic anatomical structures or non-soft tissue, like lungs or bones [70, 157].

2.2 Positron Emission Tomography Images

PET is a medical imaging technique that uses positron-emitting radiopharmaceuticals to visualize and quantify metabolic activity in the human body. These images offer a functional view of the body, revealing how different organs and tissues function at the molecular level [206].

A specific radiopharmaceutical, such as glucose radiolabeled with Fluorodeoxyglucose (FDG), is injected into the patient during this examination. This radiopharmaceutical accumulates in cells with high metabolism, such as tumors, areas of inflammation or infection, or regions with intense brain activity. Next, a specialized detector detects the radiation emitted by the positrons, allowing images to be obtained that map the distribution of the radiopharmaceutical in the body [28].

PET has several advantages, such as identifying tumors and other abnormalities in early stages, studying specific metabolic processes such as glucose consumption, protein synthesis, or cell proliferation, and quantifying the metabolic rate, providing valuable information for diagnosing and monitoring diseases [171].

This modality can be used to detect and characterize tumors, evaluate the response to treatment, and monitor disease progression. It can also study cerebral blood flow and neurodegenerative disorders, assess myocardial perfusion and ischemic heart disease, detect and locate infections, and evaluate the antimicrobial response [41, 186].

2.2.1 Positron Emission Tomography Basic Principles

PET is based on detecting positrons. These subatomic particles have a positive charge and a short half-life. They are emitted by radioisotopes injected into the patient's body linked to biologically active molecules, such as glucose or cholines. For FDG the half-life is 109.8 minutes [43].

When radioisotopes decay, they release positrons that collide with nearby electrons, generating pairs of gamma photons that move in opposite directions. However, these gamma photons are not emitted directly from the atomic nucleus but from the space

surrounding the electron-positron pair.

The key to image formation in PET lies in the coincident detection of the gamma photons. Specific detectors, such as sparkling NaI(Tl) or LaBr3(Ce) crystals, capture gamma photons and convert the energy into visible light. The scanners are constructed from several small detectors in adjacent rings around the patient door [119].

These detectors are high-density crystal scintillators that convert the energy of photons into light and are optically coupled to devices that convert light into amplified electrical signals [46], typically a photo-multiplier, PMT, and they convert radiation into detectable light, allowing the visualization of physiological and pathological processes in the human body. This process is called luminescence.

There are two types of luminescence: phosphorescence, where light is emitted for a relatively long time after excitation, and scintillation, characterized by a brief burst of light emission after excitation. The last one is more commonly used in nuclear medicine [162].

The radiation incident on the scintillator interacts with the material's atoms, exciting electrons to higher energy levels. Those excited electrons return to their ground state, releasing energy in the form of visible light. The scintillator emits light, which is then detected by a specific detector [184].

Positron emitters emit neutron-deficient isotopes. This emission is known as $\beta+$ decay, an isobaric decay process where the proton present in the emitted unstable isotope transforms into a neutron and emits a proton and a neutrino (ν_e) [206].

However, emission is not the only way for isotopes to turn into a stable element. Another way to achieve stability is through electron capture. This second phenomenon occurs for isotopes with an energy difference of less than 1.022 MeV between it and its daughter element [62].

Positron emission is more common for nuclei with low atomic weight. Equation 2.8 is the equation of a common positron decay

$$ {}^{A}_{Z}X \rightarrow ({}^{A}_{Z-1}Y + e^{+} + \nu_e) \tag{2.8} $$

the neutrino resulting from decay is a subatomic particle with negligible mass emitted without interacting with the external environment.

On the other hand, the positron interacts highly with the environment and travels a small distance, depending on its energy. This process is described in Equation 2.9

$$ e_p + \nu_e = \Delta e - 1.022 MeV \tag{2.9} $$

where e_p is the energy of the positron, ν_e is the neutrino energy, and Δe is the transition

energy.

When positrons are emitted, their motion is slowed down by the clouds of electrons in the medium until they lose their energy entirely and combine with electrons. When this occurs, an unstable element known as positronium is formed. The positron and electron annihilate each other in a fraction of a second, emitting two gamma-ray photons with a direction of approximately 180° [62].

Gamma rays are identified in PET detectors and are recorded if they arrive in a specific time window, typically in the nanosecond range. They are not recorded if the lightning strikes with a difference greater than the acceptable time window [98].

The time between the emission of the two gamma photons is crucial. If the time between photon detection is very short (on the order of nanoseconds), they are considered to come from the same radioactive decay event. Therefore, they can be used to reconstruct the location of the radiation source [72].

The interaction between the positron and the electron is assumed to happen somewhere in the straight line between the two detectors that picked up the event. This line is called Line of Response (LOR). From Time of Flight (TOF) principle, it is possible to estimate the point of the event in the LOR. The lower the TOF, the more precision in the position as shown in Equation 2.10,

$$\Delta x = c\frac{\Delta t}{2} \tag{2.10}$$

where ΔX is the LOR, c is the velocity of light, and Δt is the TOF. This generates better contrast and sensitivity [12].

CT data are used to calculate attenuation correction for PET scans and to provide anatomical information. In CT systems, the power of the X-rays is transferred to the X-ray tube through high-voltage cables wound around a set of pulleys and drums. With each 360° turn of the gantry in each direction, an image (slice) is formed. In each cut, the patient's bed is moved forward at an increment equal to the thickness of the cut [153].

Based on the information on the arrival time of gamma photons at the detectors and the geometry of the PET system, complex mathematical algorithms are used to reconstruct the image of the distribution of radioisotopes in the patient's body [62].

This reconstruction considers several factors, such as the probability of gamma photons interacting with matter, the attenuation of radiation in tissues, and the spatial resolution of the detectors [176].

2.2.2 Limitations Inherent to Positron Emission Tomography

The spatial resolution of PET, in the order of a few millimeters, is still lower than that of other imaging techniques such as CT or MRI. This can make seeing smaller anatomical details, such as small tumors or lesions, difficult. For this reason, PET must be integrated with other imaging exams and clinical data for a complete patient assessment mapping the metabolic information [153].

PET involves injecting radioisotopes into the patient's body, exposing the individual to ionizing radiation. Although the radiation dose is relatively low, this exposure must be considered and weighed against the benefits of the exam. The availability of PET scans can be impacted by limitations in the production and distribution of specific radioisotopes in certain regions [21].

2.3 Positron Emission Tomography within a Magnetic Resonance Device

As already evidenced, the images of MR allow the visualization of the detailed anatomy of the body but do not provide direct information about the metabolic activity of the tissues. Additionally, they may have difficulty distinguishing between areas of inflammation and tumors, as both may have similar features on imaging [178].

On the other hand, PET/CT involves the use of X-rays, that can be harmful to health, especially in repeated examinations, has lower anatomical resolution than MRI, making it difficult to accurately locate the metabolic activity detected by PET and does not perform as well as MRI in the differentiation of soft tissues [110]. Besides that, PET/CT image is sequential and not simultaneous.

PET-MR images are acquired simultaneously, enabling detailed analysis of both anatomy and metabolic activity. Compared to PET/CT, PET/MRI eliminates exposure to ionizing radiation from CT, making it a safer option, especially for patients who require regular examinations. The images provide a more accurate differentiation between tumors and inflammation and better differentiation of soft tissues. Since PET/MRI allows simultaneous imaging protocols, motion artifacts, and misregistration are reduced [80].

PET/MRI fusion offers a more accurate diagnosis. The combination of functional and anatomical information allows the precise identification of diseases, reducing the need for invasive exams and unnecessary biopsies. It also enables the detection of diseases at early stages when treatment is most effective, increasing the chances of a cure [150, 60].

This modality makes monitoring a patient's response to treatment possible, enabling individualized therapeutic adjustments and optimizing results [51, 35]. It also provides

precise information about the location and extent of the tumor, assisting in more accurate and effective surgical planning. Due to its diagnostic capacity, it can reduce the need to perform several complementary exams, optimizing time and resources for the patient and the healthcare system [175].

PET/MRI is employed in the diagnosis and monitoring of various types of cancer, such as lung, breast, prostate, and colorectal cancer [177, 38, 123, 94, 181]. In cardiology PET/MRI can detect acute myocardial infarction and diagnosis of inflammatory heart diseases [89, 151, 154, 114, 14].

The modality can diagnose cerebrovascular diseases such as cerebrovascular accident and transient cerebral ischemia. Information about cerebral blood flow and metabolic activity makes it easier to identify the affected area and assess the extent of damage. It also allows the accurate diagnosis of heart diseases, such as coronary artery disease, cardiomyopathy, and valvular heart disease [183].

It is also explored in the neurological field, allowing early and accurate diagnosis of neurodegenerative diseases, such as Alzheimer's and Parkinson's, epilepsy, frontotemporal dementia, brain tumors, and central nervous system infections [91, 84, 65]. PET/MRI fusion can aid in the diagnosis and localization of the epileptic focus in patients with medication-refractory epilepsy [127].

Assessment of brain metabolic activity during epileptic seizures provides valuable information for planning surgery or other treatments. PET-MR fusion images can assist in the investigation of psychiatric illnesses, such as depression, bipolar disorder, and schizophrenia. Assessing metabolic activity in different brain areas can provide clues about the disease's mechanisms and aid in treatment planning [18, 139].

2.4 Changes in PET and MRI for PET/MRI fusion

PET/MRI sites planning must predict the scanner requirements, radiopharmacy or hot laboratories, uptake rooms, and waiting rooms. Conducting a suitable environmental test of vibration suitability and magnetic homogeneity is necessary [86].

Shielding in a PET-MR facility has to restrict magnetic field and radiation emission. The exam room walls need four layers of shielding. The outer layer is the lead in radiation shielding, followed by steel for magnetic shielding and air for acoustic shielding. The inner shielding is copper for radiation shielding [45].

MRI facilities are based on four zones. Zone 1 is the area outside the facility accessible to the public. Zone 3 is the control room. Zone 4 is a magnetic room. Zone 2 is the area between Zones 1, 3, and 4, different from MRI facilities due to the radiation factor. The

scanners produce airborne and structural noise equivalent to a jackhammer. The door ceiling material must have acoustic attenuation [47].

The scanners are also sensitive to vibration, even from people walking and the traffic outside. Therefore, the floor must be designed to isolate such vibrations. The helium must be comprised of a -260 degC. The exit environment must be located where no people are around because of the high force expected during quench (1 kN force) [86].

Several solutions or configurations of PET/MRI exist. The first is to separate PET and MRI systems linked by a single patient table. The second is to place PET in MRI system. And the entire PET system could be integrated into the MRI [85].

There are four commercially available systems: the Signa PET/MRI, from GE, that uses a 3 T MR magnet with SiPM detector directly coupled to lutetium-based crystals; the Biograph mMR from Siemens uses a 3 T magnet integrated with APD detectors and lutetium oxy orthosilicate crystals; the PMR 790 from Tecnomed is a 3 T magnet with SiPM detectors directly coupled to LYSO crystals; and the Ingenuity TF PET-MR from Philips, that is a 3 T magnet with a LYSO and PMT-based PET. The images used in this study are from Siemens device, in which PET and MRI are fully integrated [44].

PET system comprises a ring of sparkling detectors that capture the gamma photons emitted by radioisotopes injected into the patient. Traditionally, PET systems design uses PMT. However, PMTs are highly susceptible to even small magnetic fields [198].

Avalanche Photodiodes (APD) are semiconductor devices that also convert light (in this case, scintillation light) into electrical signals, but with higher sensitivity than PMT. APD is integrated with a unique crystal material that emits light upon gamma ray interaction. This eliminates the need for bulky PMT and allows for a more compact design suitable for integration within an MR scanner [64, 63].

2.4.1 Challenges in PET/MRI Integration

MRI uses three types of magnetic fields generated by three types of coils: static magnetic field, gradient magnetic field, and radiofrequency field. However, PET front-end (F/E) circuits are prone toRF interferences. PET scanner systems cause changes in the homogeneous magnetic field [6].

The spatial resolution of PET/MRI is limited by several factors, such as the size of the sparking detectors in PET, the strength of the magnetic field in MRI, and the duration of the RF pulses. Besides, background radiation emitted by PET can affect MRI sensitivity, especially in regions with low metabolic activity [77].

During image acquisition, gamma rays emitted by tracer radioisotopes are absorbed

by tissue, causing image attenuation. Different tissues have different attenuation levels. Dense tissues, such as bones and muscles, attenuate gamma rays more than less dense tissues, such as fat and air. Patients with greater body mass have more attenuating tissue, leading to more significant overall attenuation on the PET image [202].

Image attenuation can lead to loss of spatial resolution and distortion of the PET image, making interpretation of results difficult. Non-uniform attenuation of gamma rays can lead to underestimation of metabolic activity in areas with high attenuation and overestimation in regions with low attenuation [172].

Attenuation correction techniques minimize the impact of attenuation on the PET image. These techniques use MRI information, gamma ray attenuation, and correct the PET image. Improved algorithms can consider image attenuation during reconstruction, resulting in higher-quality images [131].

The high cost of purchasing and maintaining PET/MRI equipment limits access to the technology for some medical centers and patients. The exam can have longer durations than individual PET or MRI scans, which may cause discomfort for some patients and increase the time required for imaging appointments at centers equipped with this technology.

3 Image Reconstruction and Compressive Sensing

In this chapter, I will make a literature review and theoretical foundation about signal processing, sampling, image reconstruction, and CS. This discussion is important to provide a solid foundation for the fundamental concepts of this work.

First, I will provide a brief overview of signal processing and the importance of time-frequency-based transformation for signals. Then, I will explain the Fourier series and its representation of discrete signals.

After explaining these basic concepts, I will describe the reconstruction process. This section will cover the theory of image reconstruction, what is established in this field, what the literature presents about the main reconstruction methods and the main challenges in the area.

Lastly, I will talk about CS theory, sparse transforms, what is already established, what the writers agree upon, and what they do not agree. Next, explain the pre-filtering process and the use of PI to reduce the number of samples required in the measurement process. Then, show where CS is used with PI and where it is not used. Finally, I will explain my purpose in overcoming reconstruction challenges using CS and PI.

3.1 Signal Processing and Sampling

In this chapter, I will make a literature review and theoretical foundation about signal processing, sampling, image reconstruction, and CS. This discussion is important to provide a solid foundation for the fundamental concepts of this work.

First, I will briefly overview signal processing and the importance of time-frequency-based transformation for signals. Then, I will explain the Fourier series and its representation of discrete signals.

After explaining these basic concepts, I will describe the reconstruction process. This section will cover the theory of image reconstruction, what is established in this field, what the literature presents about the main reconstruction methods and the main challenges

in the area.

Lastly, I will talk about CS theory, sparse transforms, what is already established, what the writers agree upon, and what they do not agree. Next, explain the pre-filtering process and the use of PI to reduce the number of samples required in the measurement process. Then, show where CS is used with PI and where it is not used. Finally, I will explain my purpose in overcoming reconstruction challenges using CS and PI.

Signal processing is a field of engineering and mathematics dedicated to analyzing, manipulating, and transforming signals, seeking to extract valuable information and make decisions based on it. A signal can be described as information that can be numerical or not. For instance, the voice is a signal transmitted by the human vocal cords. How a signal varies determines if it is discrete or continuous. Using the previous example, the voice is a constant signal.

This field is explored in telecommunications, where signal processing is used to transmit and receive information efficiently and reliably in communication systems such as cell phones, radio, and television; in the audiovisual field, to manipulate audio signals for audio editing, music compression, improving the quality of photos and videos, and performing tasks such as edge detection, noise removal, and object recognition [124].

Systems process signals, performing mathematical operations to extract relevant information. They can be linear or nonlinear, deterministic or stochastic, and can be implemented in hardware or software. The signal processing goal is to analyze, transmit, and reconstruct a signal in a receiver accurately, rapidly, and efficiently [37]. Usually, a continuous signal is converted into a discrete signal to be transmitted.

In this work, we will work with two dimensions: time and frequency. In time domains, the amplitude evolution of a signal is distributed over time. In the frequency domain, the spectral composition of the signal is analyzed, indicating what frequencies contribute to its shape. Tools such as the Fourier Transform are used to analyze the frequency of signals.

A discrete signal is a signal that varies according to an integer quantity. On the other hand, a continuous signal, such as the voice, varies in a natural numerical quantity, the time. Figure 3.1 and Figure 3.2 represent continuous and discrete signals, respectively. You can see that the second signal represents samples of the first one.

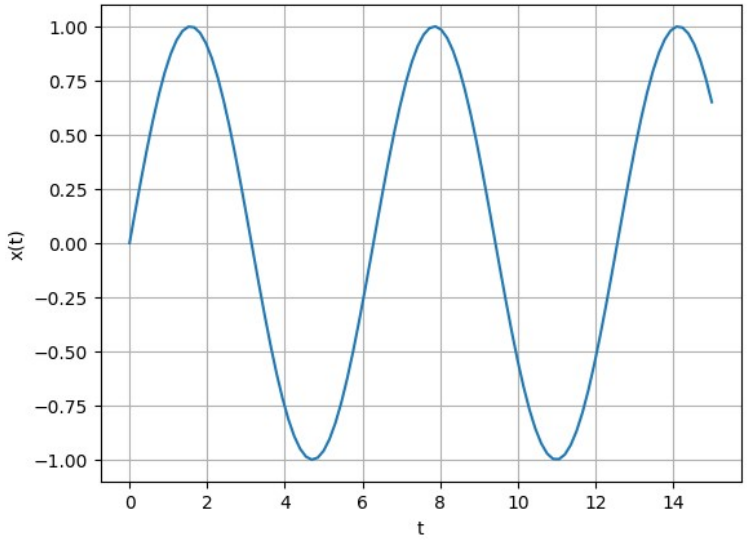

Figure 3.1. Signal continuous in the time domain. The graph presents a continuous-time sinusoidal signal. The x-axis represents time, while the y-axis represents the wave's amplitude. The wave exhibits periodic behavior, repeating itself over a fixed interval. The graph was generated using the Python programming language.

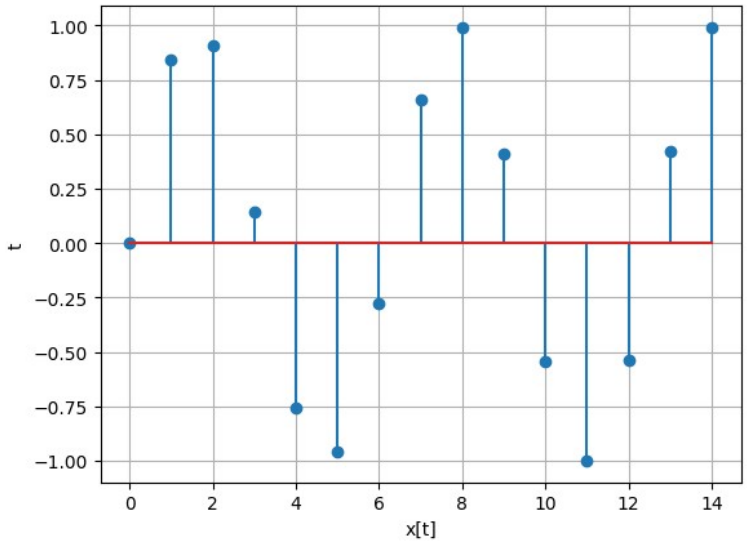

Figure 3.2. Example of a discrete-time sinusoidal signal. The graph presents a discreet-time sinusoidal signal. This means that the signal is defined only at specific, discrete points in time instead of a continuous signal, which is defined for all points in time. The spacing between the discrete points on the time axis represents the sampling rate.

For instance, if you take a picture of yourself on your smartphone, the camera sensors will measure only samples of your image, and your photo will be a discrete representation of you. To recover the continuous signal after its transmission, it is necessary to respect some conditions; those conditions are the sampling theorem [133]. To understand this, I

will talk about the Fourier transform.

3.1.1 Fourier transform

In the XVII century, the French mathematician and physicist Jean Baptiste Joseph Fourier demonstrated that any waveform can be represented through a sum of complex exponentials. The series can be used to describe periodic signals in terms of complex exponentials, in addition to being a tool for analyzing linear and time-invariant (LIT) systems [141].

Despite its good usefulness for representing signals, the Fourier series is limited to periodic signals. To overcome this limitation, the Fourier transform allows non-periodic signals to be represented in the frequency domain [140].

The Fourier Transform allows the analysis of time-varying signals through a linear combination of the signal with the complex exponential for all frequencies. The Equation 3.1

$$X(f) = \int_{-\infty}^{+\infty} x(t)e^{-j2\pi ft}dt \tag{3.1}$$

is the Fourier transform representation of a signal x(t) and Equation 2 3.2

$$x(t) = \int_{-\infty}^{+\infty} X(f)e^{j2\pi ft}df \tag{3.2}$$

represents the inverse transform.

Like the Fourier series, the transform has an even real part and an odd imaginary part for real numbers. So, if x(t) is an even signal, the transform will only have the complex part; if the signal is odd, the transform will only have the real part.

The range of signal frequencies is called signal bandwidth and can be found in Equation 3.3

$$BW = W_{max} - Wmin \tag{3.3}$$

W_{max} and W_{min} are the bandwidth's maximum and minimum frequency values, respectively.

3.1.2 Sampling

In the sampling process, a continuous signal is converted to a discrete signal, representing the signal at specific instants of time. The sampling rate determines the fidelity of the discrete representation [120]. The signal is then quantized, and amplitude is assigned to discrete values. Sampling theory defines the principles that guide converting

continuous signals into discrete representations [134].

To better understand the sampling theorem, imagine that the discrete representation of a signal $x(t)$ is $x(n)$ given by Equation 3.4

$$x(n) = x_a(nT) \tag{3.4}$$

where $x_a(nT)$ is a sample of $x(t)$ and T is the period. Let's define $x_i(t)$ as a signal in the continuous domain and given by Equation 3.5

$$x_i(t) = \sum_{n=-\infty}^{\infty} x(n)\delta(t - nT) \tag{3.5}$$

where δ is the impulse function. If we substitute $x(n)$ in Equation 3.4 in Equation 3.5, we obtain Equation 3.6

$$x_i(t) = \sum_{n=-\infty}^{\infty} x_a(nT)\delta(t - nT) \tag{3.6}$$

in wich $x_i(t)$ is zero whenever t is not a multiple of T.

In Equation 3.7

$$p(t) = \sum_{n=-\infty}^{\infty} \delta(t - nT) \tag{3.7}$$

We assume $p(t)$ as the impulse train, so we can rewrite Equation 3.6 as Equation 3.8

$$x_i(t) = x_a(t)p(y) \tag{3.8}$$

The Fourier transform of $x_i(t)$ is given by Equation 3.9

$$X_i(f) = \sum_{k=-\infty}^{\infty} X_a(f - j\frac{2\pi}{T}k) \tag{3.9}$$

where X_a is the frequency representation of x_a, $x_i(t)$ spectrum are copies of X_a distributed in a interval of $\frac{2\pi}{T}$. This shows that in order to avoid that one sample overlaps another, the distance between them has to respect the condition given by Equation 3.10

$$f_s > 2f_m \tag{3.10}$$

where f_s is the sampling frequency and f_m is the signal bandwidth.

The Nyquist Theorem, also known as the Nyquist-Shannon criterion [160], establishes that the condition established in Equation 3.10 is sufficient to capture all relevant information from a signal, the sampling rate must be at least twice its maximum frequency.

3.2 Compressive Sensing

Various signals, such as images, can be compressed to save storage memory. If a signal has elements small enough to be disregarded during transmission, it can be compressed [27].

Many signals have a sparse representation in a given domain, such as the transformed domain. If these signals can be compressed without all their components, their representation with fewer samples might be possible.

CS proposes a paradigm for data acquisition, allowing the reconstruction of signals from a reduced number of samples, lower than the amount required by the Nyquist-Shannon approach [115]. Imagine a one-dimensional signal x with size N. It is possible to reconstruct x with a number l of measurements, where

$$l < N, \tag{3.11}$$

if x has a sparse representation in a known domain, like in Figure 3.3.

Figure 3.3. Example of a sparse signal, where the colored squares represents the non-zero positions of a sparse signal. The ilustration of x_{Nx1} represent a sparse signal, and $\hat{x}_{lx1}$ is its compressed representation.

In other words, if three conditions are met, it is possible to calculate a signal x_{Nx1} from x $l < N$ linear measurements. The first one is that

$$\hat{x} = Tx, \tag{3.12}$$

where $\hat{x}$ is the sparse representation of x, and T is a known domain. The second condition

is that l cannot be smaller than the sparsity limit but must be smaller than N. The last condition is that the measurement process must be incoherent with T.

For that reason, we seek to obtain an x given by

$$Mx = b, \tag{3.13}$$

where M is the measurements matrix, and b represents the signal l non-zero components. Equation 3.13 has infinite solutions. We must choose the sparsest one. Ideally

$$\hat{x}^* = argmin_{\hat{x}} \left\| \hat{x} \right\|_0, \tag{3.14}$$

such that

$$MT^{-1}\hat{x} = b, \tag{3.15}$$

and

$$x^* = T^{-1}\hat{x}^*, \tag{3.16}$$

where T is the sparsifying transform. This solution has combinatorial complexity because, to solve it we must test all $\hat{x}$ possible non-zero elements' positions and, for each one, see if the corresponding reduced system accepts solution. After that, we choose the sparsest one. This solution is called the l_0 minimization.

There are other minimizations to get around this problem. The minimization l_1 can be seen as a convex relation of Equation 3.14. In complex cases, the solution is equivalent to a canonical program of the Second Order [55], and its solution is computationally viable.

A simpler solution would be to minimize l_2

$$\hat{x}^* = argmin \left\| \hat{x} \right\|_2^2, \tag{3.17}$$

such that $\hat{x}$ respects Equation 3.13, and

$$\left\| \hat{x} \right\|_2 = \sqrt{|\hat{x}_1|^2 + |\hat{x}_2|^2 + |\hat{x}_3|^2 + ... + |\hat{x}_N|^2}, \tag{3.18}$$

we can rewrite the Equation 3.14 as

$$\hat{x}^* = argmin_{\hat{x}} \hat{x}^H \hat{x}, \tag{3.19}$$

where H is Hermitian.

Assuming A as

$$A = MT^{-1}, \tag{3.20}$$

we can rewrite the Equation 3.13 as follows

$$A\hat{x} = b. \tag{3.21}$$

Given $L(\hat{x}, \lambda)$ such that

$$L(\hat{x}, \lambda) = (\hat{x}^H \hat{x})\lambda^H (A\hat{x} - b). \tag{3.22}$$

If we find a point where the gradient of the lagragian cancels out, we have

$$\hat{x}^* = A^H (AA^H)^{-1} b, \tag{3.23}$$

which is the representation that minimizes l_2 given the infinite solutions to Equation 3.21. The l_2 solution does not provide good results for the type of image studied in this research because it minimizes energy. The solution that minimizes non-zero coefficients would be l_0, l_1, and l_p.

The sparsifying transform represents the original signal in a sparse representation in a given domain. This transformation seeks a representation basis where relatively few non-zero components can represent the original signal. Several transforms can be used as sparsifying transforms in CS, for instance, Fourier and Wavelet Transforms.

However, applying sparse transforms can increase the computational complexity of CS algorithms, particularly for large datasets. For that matter, pre-filtering can be a helpful technique. Pre-filtering consists of applying a filter to the original signal before compressive acquisition. This filter aims to improve the signal's sparsity in the transformed domain [118].

Another tool can be used to help optimize the reconstruction process with CS, the PI. PI refers to prior knowledge about the acquired signal. This information can help limit the set of possible solutions for signal reconstruction, facilitating the process and increasing accuracy. This information can be from the signal structure, nature, statistics, or related data [118].

3.3 PET-MR Image Reconstruction

The reconstruction of images in PET-MR is a crucial step to obtain quality results for clinical use. The combination of PET with MRI offers several advantages, such as simultaneously obtaining functional and anatomical information. However, the reconstruction of the resulting images presents unique challenges due to the nature of the data acquired by each modality [73]. Several reconstruction methods have been developed to overcome these challenges.

The first MRI were acquired using an iterative reconstruction algorithm. Then the Fast Fourier Transform (FFT) began to be used. InCT, image reconstruction is accomplished using projection data. When the projection data is sufficiently comprehensive, Filtered Back Projection (FBP) techniques generate high-quality images [200].

In some cases, MRI reconstruction approaches seek to exploit temporal and k-space correlations. In other cases, they use parallel imaging techniques or exploit temporal correlations, interpolating data in the time dimension [132].

In PET/MRI case, iterative techniques are used with minimization of the difference between the raw data and the reconstructed projections [166, 26], with the use of a priori information, such as anatomical images or tissue models, to improve image quality and reduce noise [188, 138] or even with the use of physical or statistical models of the emission and detection process to generate more accurate images [26].

The Ordered Iterative Reconstruction (OSEM) method uses an iterative process to estimate the spatial distribution of tracer radioisotopes in the body, considering the probability of each photon being detected in a given detector [51, 35, 94]. It is a robust and well-established algorithm with good convergence and overall image quality [14, 127, 181]. The method has a shorter processing time than others, but it may introduce stripe artifacts in the final image, especially in areas with low photon counts [183, 172, 131].

Expectation maximization a posteriori is another option for image reconstruction. It incorporates additional information into the reconstruction, such as MRI anatomy, to improve image quality and reduce noise [51, 35, 94]. It can significantly reduce noise in the final image, especially in areas with low photon counts, and reduce streaking artifacts in the final image, resulting in a smoother, more homogeneous image [14, 127, 181]. However, it generally has a longer processing time than OSEM, which can be an obstacle for real-time clinical applications [183, 172].

3.3.1 Compressive Sensing Applied to PET/MRI

CS exploits the sparsity property of PET and MRI signals. Instead of acquiring all signal samples, it collects only a smaller subset of samples and then uses mathematical algorithms to reconstruct the complete signals [30, 82].

With this technique, imaging can significantly reduce exam time, making PET/MRI more accessible for patients with claustrophobia, children, or the elderly. It also can reduce the radiation dose to which patients are exposed during the PET scan, decreasing the risk of side effects. In the hardware, CS can be used to reduce the number of detectors in the PET scanner ring, reducing the cost, size of the equipment, and interference in MRI magnetic field.

Reconstruction of PET/MRI images with CS presents specific challenges due to the noisy nature of PET data and the complexity of integrating anatomical and functional information. Several reconstruction algorithms have been proposed to address these challenges, including $l1$-norm minimization algorithms, iterative reconstruction algorithms, and CNNs [195, 196].

3.4 Research Problem

PET combined with MRI in a single scanner is a powerful tool in the medical scenario. However, this technology still faces challenges and limitations that must be overcome for its full potential. The machine has a high cost for acquisition and maintenance. This limits the availability of these systems in many imaging centers. Merging data from the two modalities requires complex software, hardware, and a highly trained team to operate and interpret the exams. PET/MRI scans typically require longer acquisition times compared to PET/CT scans. This can be uncomfortable for the patient and limit their application in some cases [40].

Strong magnetic fields in MRI can interfere with detecting annihilation events in PET, generating image artifacts. In addition, patient movements during the examination can cause distortions in the images [11]. Joint interpretation of images requires specialized knowledge on the part of both radiologists and nuclear physicians.

The perfect overlapping of the PET and MR images is fundamental for a correct interpretation. Registration algorithms are used for this purpose but can be complex and noise-sensitive [204]. Accurate quantification of radioactive activity in PET images is critical for disease diagnosis, and follow-up [185]. The presence of the magnetic field can affect the calibration of the PET detectors, making quantification difficult [105, 100].

This research aims to evaluate the objective improvement of MRI images reconstructed from PI of PET images, acquired simultaneously and in sections with the same approximate position. Through a controlled experiment, the SER and SSIM relationships of the reconstructed images were compared, using a CS algorithm, with l_p minimization.

The relevance of this study lies in the fact that reconstructing MRI images with PI from PET can reduce the number of measurements required during the acquisition process, making the examination faster and avoiding noise caused by patient movements. A literature review shows a gap in the research on using PI from one modality to another, with cuts in nearby regions associated with CS with minimization l_p.

3.5 Related Work

In the context of medical imaging, CS has shown promise to reduce the acquisition time and radiation dose to patients [54, 106]. The use of PI can be incorporated into the reconstruction process through regularizers that impose constraints on the solution, such as sparsity, smoothness, or anatomical information [36].

By embedding PI over the image, such as the smoothness of the edges or the sparsity of the coefficients on a given base, it is possible to narrow down the space of potential solutions and achieve higher-quality reconstructions [118].

Learning dictionaries are trained on large image dataset to capture specific characteristics of a class of images [203]. Using these dictionaries in reconstruction makes it possible to explore the intrinsic structure of the images and obtain more accurate results.

The use of PI was used for the reconstruction of medical images with CS, reducing the number of measurements required for reconstruction, compared to the use of CS without PI [180, 116].

The combination of PET and MRI in a single imaging system offers a powerful synergy for the visualization and quantification of biological processes. In PET/MRI, PI provides a mask that restricts the reconstruction of the PET image from anatomical information obtained by MRI. It can also provide information such as tissue density and composition from MRI in the reconstruction of PET [193] images.

The use of PI can also be used in constructing kinetic models to describe the distribution of the radiotracer in the tissue over time, allowing the estimation of pharmacokinetic parameters. In addition, they can provide a training base for machine learning techniques to learn data representations [187, 143]. In [163], we observed observed that it is possible to extract PI from one modality to another from PET/MRI PI, the program used was developed for PET/CT images in [58]. The use of PI combined with image reconstruction techniques can improve the process and, at the same time, speed it up [87].

There are imaging techniques that make use of PI, extracting information from one slice to another [58] or from one frame to another [116]. In [113], PI anatomic of MRI is used to reconstruct PET images acquired from a PET/MRI equipment, and the use of CS to the methodology is evaluated. In the study, the CS method performed well in reducing artifacts. Still, it did not show good results in correcting artifacts caused by movement and having a high computational cost. However, the author suggests that further investigations can be done by optimizing the CS algorithm.

The use of PI is an important resource to improve the PET/MRI reconstruction process, and it is a factor of agreement in studies in this area. However, combining data from PET and MR can lead to disambiguation problems, especially in regions with low

metabolic activity.

4 PET-MR Imaging Proposed Method

The data was extracted from Biograph mMR, but the image set was not organized in pairs of images, nor were the images aligned. To solve this problem, I made a program to access image metadata. First, the algorithm separates images by studies, then, the studies that did not contain images from PET and MRI were discarded.

After that, the algorithm discarded images from PET and MRI that did not have the same slice orientation. Lastly, the pairs were formed by slice proximity. Once the pairs were formed, the images were aligned manually.

This work addresses the development and evaluation of a system for analyzing PET images PI extraction used in MRI reconstruction. This is the scenario of PET and MRI measurements acquired in an imaging session of the same patient. The idea is to evaluate whether there is an improvement in the reconstruction of MRI based on PET measurements obtained in the same condition of position, anatomy, and physiology under examination, compared to the usual scenario in which each image is reconstructed in isolation from the measurements corresponding to each case.

To this end, this author proposes a set of algorithms that starts with PET images reconstructed using already consolidated techniques (in this case, PET images provided by SIEMENS® were used). From these images, a set of positions of non-zero elements are extracted in the sparse representation to be used in the next step. The sequence is carried out by applying compressive sensing techniques using the linear measurements provided by the MRI equipment.

During these techniques, the idea is to explore the information already obtained from PET images and observe the reconstruction quality depending on the number of positions extracted and the number of measurements used. The expectation is that the use of PI from PET images for MRI will lead to a statistically significant increase in the objective quality of MR images, reflecting a potential gain for MRI modality due to equipment that allows parallel acquisition of measurements PET and MRI.

This chapter details aspects related to the involved algorithms implementation and the experimental procedures necessary to apply these algorithms to test image pairs provided by SIEMENS®. It also details the methods for systematic and statistical analysis

of these data, allowing the consistency of any gain in objective quality to be inferred.

In this sense, section 4.2 describes the implementation of compressive sensing algorithms with pre-filtering and the extraction of information from PET images to be used in the reconstruction of MR images. It describes the need to align PET/MRI images to apply the proposed method: the information extracted from PET images refers to the positions of specific anatomical structures present in the filtered versions of the images. Thus, its use in MRI requires that the coordinates be referred to a scale common to both modalities. Therefore, it was necessary to adapt the resolutions, positions, and alignments in each pair of images.

Section 4.3 describes the experiments carried out to statistically evaluate the proposed method. It begins with defining the PET/MRI image base used. It continues with a description of the conditions under which the MR images were reconstructed, including the types and amounts of linear measurements used (i.e., the types and densities of trajectories in k-space) and the amounts of PI used in each case.

Finally, section 4.4 describes the analysis of the results obtained with all tested images. A description is made about the objective quality metrics used, the statistical parameters of these metrics for comparison purposes in scenarios with and without the proposed PI, and the hypothesis tests used to determine statistical significance.

4.1 Research Scope

The fusion of PET and MRI images represents a significant advance in diagnostic imaging, combining the high metabolic sensitivity of PET with the excellent spatial resolution of MRI. However, accurate and efficient reconstruction of these hybrid images poses a challenge. The presence of noise due to the interference of the PET hardware in the magnetic field of MR and the interference of the magnetic field in the formation of PET images, added to the artifacts caused by the patient's movement during the examination, compromise the quality of the images acquired [17, 129, 147].

The quality of the reconstructed image directly impacts diagnostic accuracy and the ability to detect small and discrete lesions, with direct implications for therapeutic planning and follow-up of treatment response. Therefore, the scientific community has invested significantly in developing new PET/MRI imaging reconstruction techniques. Some of the approaches include machine learning, regularization, and physical models [146, 197].

The main objective of this research is to evaluate the qualitative improvement of MRI images using PI of PET, extracted from sections with approximately equal positions, with CS. The results of this research can help overcome the attenuation problems of

MRI images and reduce the exam time by reducing the number of measurements to be extracted from the MR images. From this main objective, it defines the following specific objectives:

- The use of PI information of PET images in CS algorithms can reduce the number of measurements needed to reconstruct MRI by how much?

  Observe if the use of PI of PET images in CS algorithms can reduce the number of measurements required in MRI reconstruction process.

- How many measurements are necessary to maintain MRI quality using PI information from PET images?

  Observe the minimum number of measurements necessary to maintain MRI quality using PI information from PET images.

- How many measurements are necessary to improve MRI quality using PI information from PET images?

  Observe the minimum number of measurements necessary to improve MRI quality using PI information from PET images.

- What PI percentual is necessary to maintain MRI quality in an interval of 7 angles equally spaced from 10 to 160?

  Observe the minimum PI percentage necessary to maintain MRI quality in an interval of 7 angles equally spaced from 10 to 160.

- What PI percentual is necessary to improve MRI quality in an interval of 7 angles equally spaced from 10 to 160?

  Observe the minimum PI percentage necessary to improve MRI quality in an interval of 7 angles equally spaced from 10 to 160.

- What PI percentual is necessary to reduce MRI quality in an interval of 7 angles equally spaced from 10 to 160?

  Observe the minimum PI percentage necessary to reduce MRI quality in an interval of 7 angles equally spaced from 10 to 160.

- What is the relation between PI percentage and the number of measurements?

  Observe the relation between PI percentage and the number of measurements.

- What are the maximum SER and SSIM values obtained with the proposed method?

  Observe the maximum SER and SSIM values obtained with the proposed method.

- What is confidence in the experiment's results?

  Perform a statistical analysis of the results.

This work adopted the positivist research approach. In this sense, it is based on empirical observation and logical analysis, where the facts are recorded with a neutral perspective. The experiments were conducted to test the hypotheses and see if they were compatible with the data collected.

In addition, the deductive approach was adopted. The analysis is based on deductive reasoning, starting from the fact that CS was already successfully employed in medical image reconstruction, and PI is explored in PET/MRI research.

4.2 Development Methodology

To start this research, obtaining simultaneously acquired PET and MR images was first necessary. The images were provided by SIEMENS® and extracted from the PET/MRI machine Biograph mMR®. The dataset consists of 16.197 MR images and 4.697 PET images.

Initially, the data was randomly distributed and in DICOM format. Initially, the MATLAB® function dicomCollection was used to get preview information about the dataset. Then, a Python algorithm was created to access the image metadata and separate them into folders according to the study and the modality 4.1.

The DICOM metadata filtered the files by study identification to ensure the images belonged to the same study case. Then, the images were divided according to the modality. The dataset has six studies of the knee, head, breast, and whole body 4.1. Not all studies contained two types of images. Data collection was non-random, as it is a study in which the images should belong to the same cutting position. Only the cases with both PET and MR images were selected.

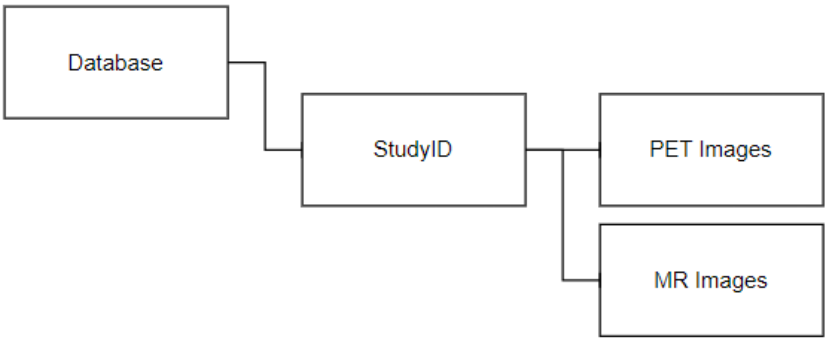

Figure 4.1. Dataset Organization Structure.

Table 4.1. Dataset studies description.

Study	Patient Age	Patient Gender
Knee	22	Female
Breast	59	Female
Head	71	Female
Whole Body	Not informed	Not informed
Whole Body	Not informed	Not informed
Whole Body	Not informed	Not informed

After that, an interface was created to examine and align the images. For this phase, a set of Python bindings, PyQT5. The interface filters the images by orientation and position. The slice positions from PET and MRI, which had the same slice orientation, were compared, and the Euclidean distance between the two slices was measured. To be considered a pair, the difference had to be smaller than 1 [163].

Once the pairs are formed, each image must be aligned. The slices are resized, rotated, and translated until PET and MR images are fully merged. Once the fusion was completed, the images in the new position were saved separately.

The saved files contain the original PET and MR images, the versions of those images once aligned, and the proportion of each spatial operation. These files are saved in MATLAB format®, and all the images from each study are saved in the same file.

After this pre-processing step, it is necessary to simulate the k-space representation of MRI for the reconstruction process. Then, the MRI goes through a pre-filtering filtering process. This step is necessary to create a sparse representation of the image. Then, I vectorize PET images and choose their highest values as PI. Lastly, the reconstruction is performed.

4.2.1 Extraction of k-space measurements from the MR images

For each MR image provided by SIEMENS®, different sets of measurements were initially extracted in the k-space to evaluate CS reconstruction in different scenarios (with and without PI from PET images).

One might think that this procedure is redundant because we already have the image. However, obtaining k-space measurements allows us to reconstruct MR images, but at different conditions, with different amounts of measurements and using or not information from PET images. The manufacturer has access to the original measurements; in this case, we must recalculate them based on the images.

The MRI machine provides the image representation in the Fourier domain along a trajectory. This representation takes place in k-space. In this experiment, we considered

the radial trajectory to extract the measurements, which is a good compromise between quality and complexity.

To simulate the measurements of the MRI machine, a Python function was implemented that, based on the image dimensions and the various inclination angles between the radial lines, returns the positions of the points along the trajectory. In other words, this function returns the positions of the information that the MRI machine provides along the trajectory.

The inclination angles are equally spaced, varying from 0 to π. They determine the number of radial lines that the trajectory will have. Once we have the positions, we calculate the Discrete Fourier Transform (DFT) of the MR image and take measurements only at the points of the radial trajectory. This is the representation of the measurements returned by resonance.

We assessed the objective quality of the reconstructed images with 5 angles varied in a range of 10 to 135. The fewer angles, the shorter the reconstruction time. However, the image quality is compromised. It is evaluated whether using CS improves image quality, even at a low number of angles.

4.2.2 Compressive sensing with pre-filtering applied to MRI images, without prior information from PET images

According to [179], the pre-filtering process is beneficial for the reconstruction process from a reconstruction quality and time point of view. The image is decomposed using 2D Haar filters Equações 4.1 e 4.2.

$$h_1 = h_2^T = \begin{bmatrix} 1 & 1 \\ -1 & -1 \end{bmatrix} \tag{4.1}$$

$$h_3 = \begin{bmatrix} 1 & -1 \\ -1 & 1 \end{bmatrix} \tag{4.2}$$

As a result of this operation, three images are obtained. Each one of them represents high-frequency information in one direction. This way, one has a sparse image with high frequencies at the horizontal, another at the vertical, and another at the diagonal direction. The DC level is represented by the trajectory information obtained from the MR scanner.

4.2.3 Extraction of prior information from PET images for reconstruction of MRI images

PI is a set of non-zero element positions on sparse representation. In this case, each filtered version of the image is its sparse representation. It has already been shown on [179] that if additional information on the support sparse domain is taken, fewer samples on the time domain are needed.

This information can be used to eliminate ambiguity because more than one sparse vector can lead to the solution. Using this extra information, different vectors might lead to the same initial samples but in various positions.

The main goal is to obtain an MRI reconstructed with PET image information. To do this, both MRI and PET images have to be aligned. Since the images had different resolutions and coordinates, they must be aligned first. This process was possible because of an interface that compares the images and allows the user to rotate, resize, and shift the images in horizontal and vertical directions [163].

In the case of PET/MRI equipment, the manufacturer has access to information about the positioning of the sensors concerning the patient and the differences between the positions used in both cases. They also have access to the image resolutions used. This allows the conversion of positions and resolutions from one modality to the other.

This information is extracted from PET by obtaining the highest spectrum values. In other words, the PET DFT is calculated, then the 2D spectrum is stacked in a 1D spectrum. After this process, the signals are sorted in a decreasing fashion, and finally, the highest signals are taken.

The reconstruction process is performed after one has the PI and the three decomposed images. Since the three representations are independent, they can be reconstructed in parallel. The result is obtained by applying a spectrum composition of the images.

4.3 Experimental Procedures

Once the pairs of images were formed and aligned, they were ready for experimentation. As the images contained did not have $k - space$ information, it is necessary to simulate these data.

One of the hypotheses to be investigated was whether the extraction of PI from PET images to reconstruct MR images with CS would enable the reconstruction process with fewer measurements. Changes were then made to the number of measurements, and the quality of the reconstructed image was evaluated.

To evaluate the quality of the images, SER and SSIM were used. The first metric measures the relationship between the proper signal (the original image) and the noise present, i.e., the amount of noise in the image. And it corresponds to the ratio between signal and noise power. A high SER value indicates a low-noise, high-quality image.

The second metric evaluates the structural similarity between two images, considering luminance, contrast, and structure. A value of SSIM close to 1 indicates that the images are very similar. This metric better captures the human perception of image quality, considering aspects such as blur, noise, and distortions.

The evaluation of SER in a complementary way to SSIM allows us to obtain complementary information on the noise and structural similarity of the original and reconstructed images.

The SER and SSIM relationship between the reconstructed images and the original image were collected for each scenario. In addition, the processing time was also recorded.

In addition, the effect of the amount of PI extracted from PET on the final result was observed. Tests were made for various percentages of PI, in all cases of different amounts of MRI measurements. All results were collected at the end of each reconstruction process.

4.4 Methods for Results Analysis

After data collection, descriptive techniques were applied to summarize the data and identify initial patterns such as mean.

To determine the most appropriate statistical test, we used the normality analysis of the SER data, both for images with PI and those without PI. The Shapiro-Wilk and Kolmogorov-Smirnov tests were used to verify the data's adherence to a normal distribution, with the null hypothesis (H0) that there is no significant difference between the means of SER with 10 % of PI and without PI.

Normality was rejected, so we used the Wilcoxon test for paired samples. The Wilcoxon test is a non-parametric test that does not assume normal distribution for the data, being more robust in situations where normality cannot be guaranteed. The p-value was calculated to assess the statistical significance of the difference between the means or medians. Next, we compared it with the significance level: the p-value obtained was compared with the pre-defined significance level of 0.05.

The descriptive analysis summarized and described the data concisely, using measures of central tendency (mean).

5 Results and Discussion

Reconstruction of PET/MRI is a complex and fundamental process for obtaining high-quality medical images. However, problems such as artifacts and noise can compromise image quality, impacting medical diagnosis.

This chapter aims to present and discuss the results obtained from analyzing the data collected in the research. This study aimed to investigate the relationship between the objective quality of the reconstructed MR images, the number of k-space radial lines, and the percentage of PI extracted from PET images used in the reconstruction process.

Given this, the questions and objectives of this research will be specified again. Next, the characteristics of the sample images used in the experiments will be described as the descriptive and inferential analysis of the data obtained and, finally, the relationship between the variables. To contextualize the results, comparisons will be made with previous studies and the hypotheses raised in the theoretical chapter.

With this study, I aim to answer the following question: "What is the SER and SSIM obtained when applied PI from PET images combined with CS algorithms to reconstruct MR images?" This question can be further specified, and from it, other questions were extracted, and from these, specific objectives can be defined, such as:

- The use of PI information of PET images in CS algorithms can reduce the number of measurements needed to reconstruct MRI by how much?

  Observe if the use of PI of PET images in CS algorithms can reduce the number of measurements required in MRI reconstruction process.

- How many measurements are necessary to maintain MRI quality using PI information from PET images?

  Observe the minimum number of measurements necessary to maintain MRI quality using PI information from PET images.

- How many measurements are necessary to improve MRI quality using PI information from PET images?

Observe the minimum number of measurements necessary to improve MRI quality using PI information from PET images.

- What PI percentual is necessary to maintain MRI quality in an interval of 7 angles equally spaced from 10 to 160?

  Observe the minimum PI percentage necessary to maintain MRI quality in an interval of 7 angles equally spaced from 10 to 160.

- What PI percentual is necessary to improve MRI quality in an interval of 7 angles equally spaced from 10 to 160?

  Observe the minimum PI percentage necessary to improve MRI quality in an interval of 7 angles equally spaced from 10 to 160.

- What PI percentual is necessary to reduce MRI quality in an interval of 7 angles equally spaced from 10 to 160?

  Observe the minimum PI percentage necessary to reduce MRI quality in an interval of 7 angles equally spaced from 10 to 160.

- What is the relation between PI percentage and the number of measurements?

  Observe the relation between PI percentage and the number of measurements.

- What are the maximum SER and SSIM values obtained with the proposed method?

  Observe the maximum SER and SSIM values obtained with the proposed method.

- What is confidence in the experiment's results?

  Perform a statistical analysis of the results.

The relevance of these questions lies in the need to reduce the number of measurements required for the reconstruction of MR images to reduce the acquisition time of MRI and to improve the quality of the images by mitigating noise interference in the reconstructed image. The results obtained in this research demonstrate a positive correlation between the use of PI in the process of reconstruction of MRI images and the increase in image quality, corroborating the findings in [116].

I will assess image quality using objective metrics such as SER and SSIM, as radiologist opinions were not collected for qualitative analysis. The data used in this research was obtained from the Biograph mMR, with Siemens providing access to DICOM format images for academic use.

5.1 Dataset

Although cases were selected randomly, the images used in this investigation were not chosen randomly due to the lack of study examples with pairs of PET and MR images. Since the images were in DICOM format, k-space measurements were not accessible, and I simulated k-space measurements from the available MRI.

Moreover, pairs of images were aligned based on slice position and orientation similarity, and resolution information was estimated during manual alignment. The exams evaluated are from the head region, and the slices are axial. The metadata did not have information about the patient's gender or age.

The dataset has 448 pairs of PET and MR images from several slice positions of a human head. Figure 5.1 exemplifies MR, PET, and fusion images. The MR images have dimensions ($204X384$) and PET images have dimensions ($344X344$). The image formed by the overlap of the two modalities has final dimensions of ($344X384$).

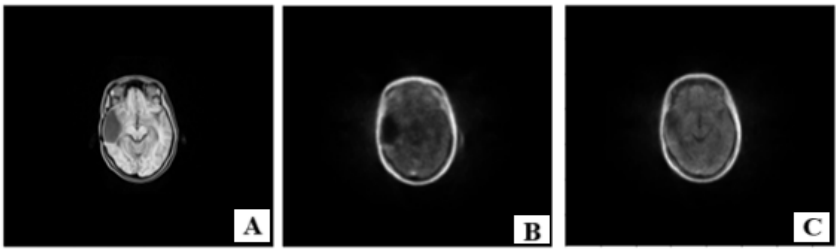

Figure 5.1. Images extracted from the dataset. Figure A is an MR image; Figure B is the PET image from the same position, and Figure C is the two images fused and aligned to form a pair of PET/MRI.

The new images are saved in a MATLAB format file with the new resolutions of both images. To avoid possible noises caused by changes in resolution, only the PET image was changed, while the MR image was kept unchanged.

5.2 Proposed Method Performance

The reconstruction was applied to the first 100 images. For each image, the reconstruction process was performed with different numbers of radial lines, and for each number of radial lines, a different portion of PI. For the experiment, an interval of radial lines angles between 10 and 135 with an interval of 25 was used, and an interval of 0 to 90 % of PI with an interval of 10 %. Figure 5.2, 5.3 contains the mean values of SER and SSIM for the 100 images in all experiment scenarios.

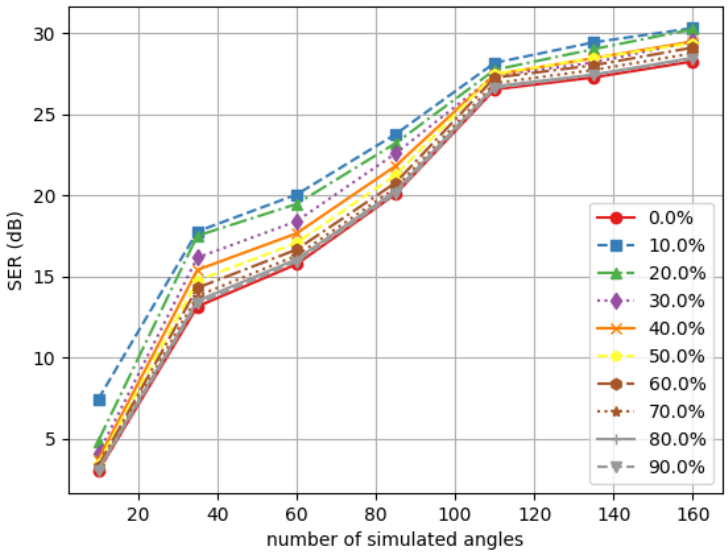

Figure 5.2. The mean values of SER of 100 images for 7 different numbers of angles equally distributed between 10 and 160. For each number of angles, the experiment was reproduced for different proportions of PI, from 0 to 10 %. Where the images reconstructed with 10 % of PI had the best SER.

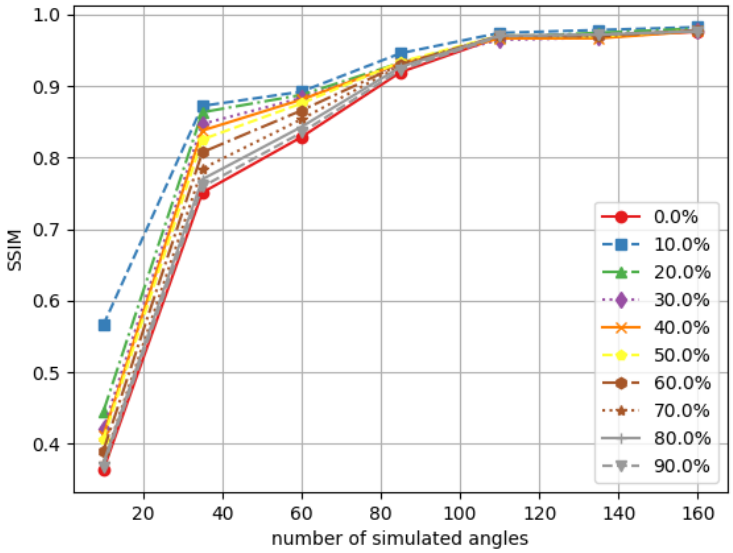

Figure 5.3. The mean values of SSIM of 100 images for 7 different numbers of angles equally distribute between 10 and 160. For each number of angles, the experiment was reproduced for different proportions of PI, from 0 to 10 %. Where the images reconstructed with 10 % of PI had the best SSIM.

To evaluate the results of changing the number of angles and the PI proportion on SER and SSIM, we used the Wilcoxon test, a non-parametric test suitable for comparing paired measures. The null hypothesis (H0) assumed that there would be no significant

difference between the measurements before and after the intervention. The test results revealed a p-value of according to Table 5.1. Considering a significance level of $p \leq 0.05$, we reject the null hypothesis, which indicates that the intervention caused a statistically significant difference in SER and SSIM. These results suggest that the new intervention was effective in improving image quality and, at the same time, reducing the number of measurements required for the reconstruction of MR images using PI of PET images acquired simultaneously.

Número de ângulos	p
10	$3.90.10^{-18}$
35	$2.79.10^{-17}$
60	$7.56.10^{-18}$
85	$1.96.10^{-17}$
110	1.90^{-14}
135	$1.56.10^{-13}$
160	$2.96.10^{-13}$

Table 5.1. Diferent values of p for tests performed between the mean SER for 100 images with 0 and 10 % of PI.

The first research question is: "The use of PI information of PET images in CS algorithms can reduce the number of measurements needed to reconstruct MRI by how much?". From the results above, it is possible to infer that the use of PI information of PET images in CS algorithms can reduce the number of measurements needed to reconstruct MRI. Figures 5.4, 5.5 and 5.6, are examples of images reconstructed without PI and with 10 % of PI. It is possible to see that with 85 angles, the image is visually better. According to Figure 5.3, with 85 angles, we can achieve a SSIM higher than 0.9.

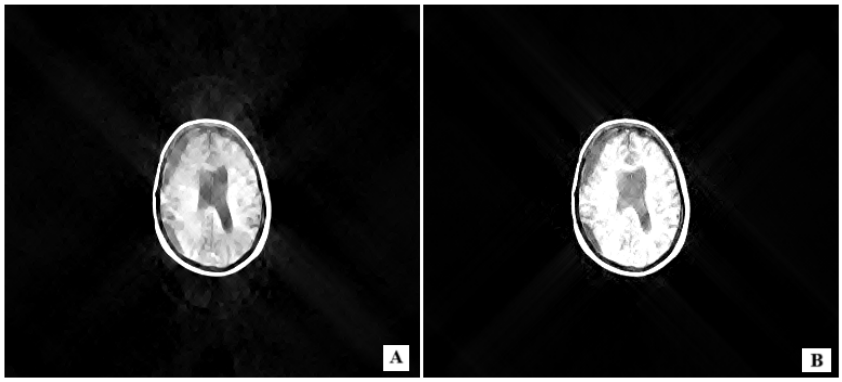

Figure 5.4. Image reconstructed with 35 angles. Figure A was reconstructed without PI, and Figure B was reconstructed using 10 % of PI.

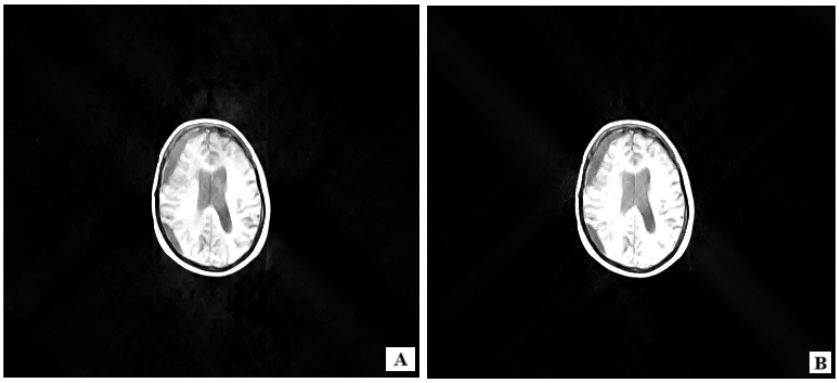

Figure 5.5. Image reconstructed with 60 angles. Figure A was reconstructed without PI, and Figure B was reconstructed using 10 % of PI.

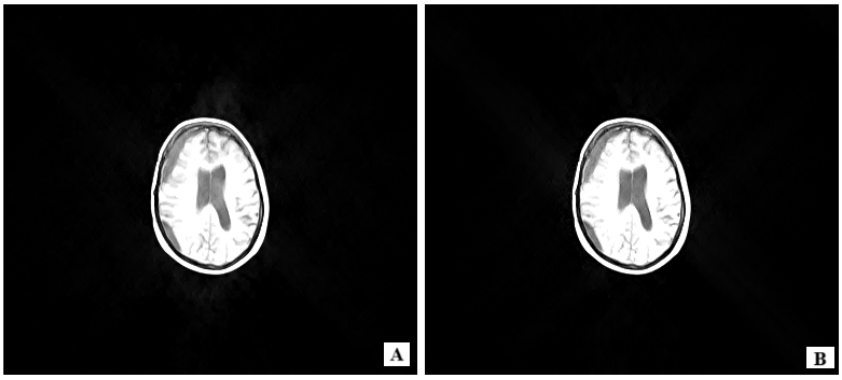

Figure 5.6. Image reconstructed with 85 angles. Figure A was reconstructed without PI, and Figure B was reconstructed using 10 % of PI.

As for the question: "How many measurements are necessary to maintain MRI quality using PI information from PET images?", we can return to Figure 5.3 and observe that after 100 angles, the value of SSIM achieve its saturation point. In Figure 5.7, we can observe this result from a qualitative point of view.

For questions: "How many measurements are necessary to improve MRI quality using PI information from PET images?" and "What PI percentual is necessary to improve MRI quality in an interval of 6 angles equally spaced from 10 to 160?", 10 % of PI improves is the proportion that showed the best results. Using 10 % of PI proportion from PET images, we can achieve at least 0.9 of SSIM with 80 angles of MRI radial lines. With more than 100 angles, the SSIM achieves its saturation point as observed in Figure 5.8.

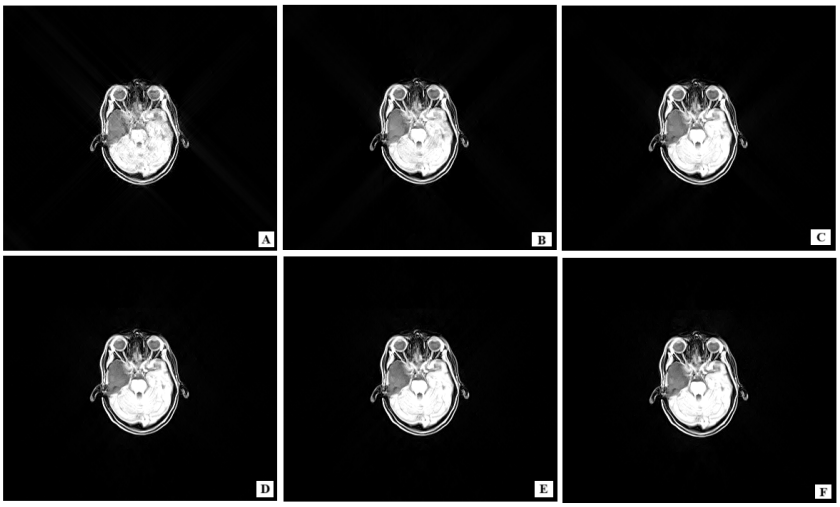

Figure 5.7. Images reconstructed with 10 % of PI for different angles. Figures A to F are the MR images reconstructed with the interval of 35 to 160 angles equally spaced. It is possible to notice that from Figure C to F the images are very similar.

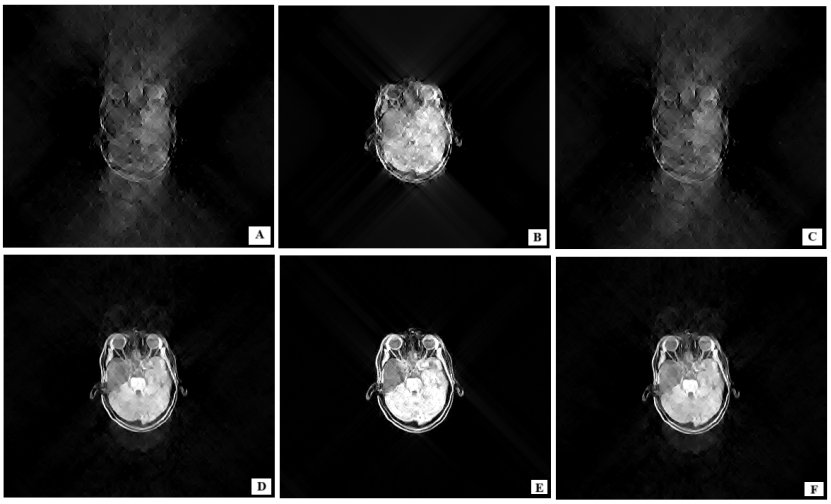

Figure 5.8. Diferent scenarios comparison. Figures A, B, and C are images reconstructed with 10 angles with 0 %, 10 % and 90 % of PI. Figures D, E, and F are images reconstructed with 35 angles and 0 %, 10 %, and 90 % of PI. It is possible to observe an improvement in quality between Figures A and B, although the images still have low resolution; in Figure C, it is clear that there was a drop in image quality. Figures D, E, and F significantly improve resolution, with Figure E having greater visual quality. This supports the hypothesis that images with 10 % of PI present better results.

The present research aimed to investigate the relationship between the number of angles and the proportion of PI used in the reconstruction of images of MR and SER and SSIM. The results demonstrate that using 10 % of PI objectively improves the quality of the images and reduces the number of measurements required for reconstruction. These findings corroborate previous studies' results that using PI combined with CS can improve image quality. However, too high a value of PI can reduce the quality of the images. This

may be related to the fact that a very high amount of PI can bring noise inherent to the support image.

The implications of these results are significant, as they suggest that it is possible to use PI images of a PET image to reconstruct MR images. This may reduce the number of measurements required for the reconstruction process.

Future research can explore analyzing processing time about the l_p optimization process. In summary, the results of this study contribute to a better understanding of the relationship between the use of PI and SER and SSIM.

6 Conclusion

The present research explores the potential of incorporating IP from PET images in the reconstruction process of MR images using CS and pre-filtering. This method helps reconstruction because PET images are extracted from the same frame and slice position as MR images.

The central hypothesis was that using IP images of different modalities simultaneously extracted from the same position and slice orientation could improve reconstructed image quality.

In the PET/MRI case, this can compensate for the noise caused by interferences inherent to the equipment and reduce the number of measurements used in the reconstruction process.

The dataset provided does not have information on the resolution and proportion between the images. Therefore, adjusting the resolution is necessary to align the images. The MR images were kept unchanged to avoid noise from resizing operations, and the PET images were adjusted to align with the MRI.

After aligning the images, the PET images were pre-filtered, using Haar filters, to obtain a sparse version of the images. Then, each filtered version was vectorized, and the positions of the highest intensity values were extracted according to the proportion of PI used in the experiment.

A k-space simulation was extracted from the original images with the number of angles corresponding to the scenario to be evaluated in the experiment to obtain the radial trajectory of the resonance images. This result was filtered with Haar filters, and each of the three versions obtained was reconstructed using CS with l_p minimization, with p = 1, and with PI extracted from the PET images corresponding to the slice position. At the end of this process, three sparse images were obtained, and the final image was formed through a spectral composition of the three images.

Experiments were performed with 100 images in different scenarios. We tested the reconstruction results by varying the percentage of PI from 0 to 90 %, with 10 equally spaced values, and the number of angles from 10 to 160, with 7 equally spaced values. We used Signal-to-noise ratio (SER) and Structural Similarity Index Measure (SSIM) for

image quality evaluation.

After collecting the experimental data and the quantitative analysis, the results showed that the use of 10 % of PI improved image quality for all scenarios tested. We used statistical tools to explore the relationships between the variables. Statistical analysis of the data collected allowed for validating hypotheses and identifying relevant patterns. Images reconstructed with 60 angles had an average SER of approximately 16dB and an average SSIM of roughly 0.82, while the images reconstructed with 10 % of PI had an average SER of 20dB and an average SSIM of approximately 0.89.

In summary, the results demonstrated that the use of 10 % of PI of PET can reduce the number of measurements required for the reconstruction process and improve the quality of MR images. These findings corroborate the results of previous studies that point out that the use of PI can improve the quality of reconstructed images and reveal that a high number of PI can negatively impact the quality of the images.

This suggests that the most intense improvements could potentially be for percentages between 0 and 10 % or between 10 % and 20 % since the gain has declined above 20 %, and no other intermediate values have been tested.

There was a significant difference compared to studies with other types of PI. In the different studies, quality declines when PI significantly increases compared to not using PI. In the case of this survey, we only observed a reduction in the gain of up to 90 % of PI. A possible explanation is that, in our case, PI refers to the same slice acquired simultaneously, although with another technology. In other studies, PI generally refers to other slices, time frames, or a set of slices.

In addition, PET images are simpler and have fewer detectable structures in the sparse versions than MRI. Hence, a high percentage of coefficients in PET images represent less content than the same percentage of PI in previous studies where it is extracted from other types of images. But this requires more investigation.

Future research may explore analyses about processing time and the optimization process or experiment for a percentage of PI above 90 %; if the quality of the images worsens the result without PI, it may be an indication that the percentage of coefficients in PET images represents less content than in other types of PI. Another point is to test PI percentages between 10 % and 20 % with smaller spacing between the values. There is also a need to investigate this methodology with other methods of pre-filtration, trajectory, and anatomical regions. The use of AI to extract PI more effectively can also be evaluated: high coefficients can always bring at least a small percentage associated with noise.

Together, the results of this study contribute to a better understanding of how the

use of PI from one modality to another can impact the process of image reconstruction with CS.

References

[1] Y. M. Y. Abdallah. History of medical imaging. *Archives of Medicine and Health Sciences*, 5(2):275–278, 2017.

[2] F. M. Abu-Zidan, A. F. Hefny, and P. Corr. Clinical ultrasound physics. *Journal of emergencies, trauma, and shock*, 4(4):501–503, 2011.

[3] A. Afaq, D. Faul, V. V. Chebrolu, and et al. Pitfalls on pet/mri. *Seminars in Nuclear Medicine*, 51(5):529–539, 2021.

[4] B. Aggarwal. *Textbook of Radiology and Imaging, Volume 1-E-Book*. Elsevier India, 2023.

[5] S. Ahangari, A. B. Olin, M. K. Federspiel, and et al. A deep learning-based whole-body solution for pet/mri attenuation correction. *EJNMMI physics*, 9(1):55, 2022.

[6] M. S. H. Akram, T. Obata, M. Suga, and et al. Mri compatibility study of an integrated pet/rf-coil prototype system at 3 t. *Journal of Magnetic Resonance*, 283:62–70, 2017.

[7] E. E. Alaa, A. S. Ashour, Y. Guo, and et al. A novel weighted compressive sensing using l1-magic recovery technique in medical image compression. *Health information science and systems*, 8(1):2–10, 2019.

[8] D. C. Alexander, T. B. Dyrby, M. Nilsson, and et al. Imaging brain microstructure with diffusion mri: practicality and applications. *NMR in Biomedicine*, 32(4):e3841, 2019.

[9] M. Amirrashedi and et al. Towards quantitative small-animal imaging on hybrid pet/ct and pet/mri systems. *Clinical and Translational Imaging*, 8:243–263, 2020.

[10] F. H. Attix. *Introduction to radiological physics and radiation dosimetry*. John Wiley & Sons, 2008.

[11] Y. Bai and et al. Deep learning-based motion correction for simultaneous pet/mri. *Physics in Medicine and Biology*, 66(18):185006, 2021.

[12] S. Basu, S. Hess, P. N. Braad, and et al. The basic principles of fdg-pet/ct imaging. *PET clinics*, 9(4):355–370, 2014.

[13] J. P. Bernd, F. W. Hans, A. Kolb, and et al. Positron emission tomography/magnetic resonance imaging: The next generation of multimodality imaging? *Seminars in Nuclear Medicine*, 38(3):199–208, 2008.

[14] G. Beyer and C. Schusterbauer. Pet/mri in cardiology. *Journal of the American College of Cardiology*, 67(12):1426–1438, 2016.

[15] T. Beyer and et al. A combined pet/ct scanner for clinical oncology. *Journal of nuclear medicine*, 41(8):1369–1379, 2000.

[16] I. Bezrukov, F. Mantlik, H. Schmidt, and et al. Mr-based pet attenuation correction for pet/mr imaging. In *Seminars in nuclear medicine*, volume 43, pages 45–59. Elsevier, 2013.

[17] B. Bogdanovic, E. L. Solari, A. V. Asiares, and et al. Pet/mr technology: Advancement and challenges. *Seminars in nuclear medicine*, 52(3):340–355, 2022.

[18] K. Borbély, M. Emri, I. Kenessey, and et al. Pet/mri in the presurgical evaluation of patients with epilepsy: A concordance analysis. *Biomedicines*, 10(5):949, 2022.

[19] W. G. Bradley. History of medical imaging. *Proceedings of the American Philosophical Society*, 152(3):349–361, 2008.

[20] C. Brendle, C. Maier, B. Bender, and et al. Impact of 18f-fet pet/mri on clinical management of brain tumor patients. *The Journal of nuclear medicine (1978)*, 63(4):522–527, 2022.

[21] G. Brix, U. Lechel, G. Glatting, and et al. Radiation exposure of patients undergoing whole-body dual-modality 18f-fdg pet/ct examinations. *Journal of Nuclear Medicine*, 46(4):608–613, 2005.

[22] M. A. Brown and R. C. Semelka. *MRI: basic principles and applications*. John Wiley & Sons, 2011.

[23] R. W. Brown, Y. N. Cheng, E. M. Haacke, and et al. *Magnetic resonance imaging: physical principles and sequence design*. John Wiley & Sons, 2014.

[24] R. N. Bryan. *Introduction to the Science of Medical Imaging (Ed.)*. Cambridge University Press, 2009.

[25] S. C. Bushong and G. Clarke. *Magnetic Resonance Imaging: Physical and Biological Principles*. Elsevier Health Sciences, 2003.

[26] J. Cabello and S. Ziegler. Advances in pet/mr instrumentation and image reconstruction. *British Journal of Radiology*, 91(1081):20160363, 2018.

[27] E. Candès and J. Romberg. Sparsity and incoherence in compressive sampling. *IOP*, 23(3):969–985, 2007.

[28] D. M. Cannon, T. J. Kruser, and D. Khuntia. Principles and application of pet in brain tumors. *PET clinics*, 6(2):131–148, 2011.

[29] C. Catana. Attenuation correction for human pet/mri studies. *IOP*, 65(23):23TR02, 2020.

[30] C. Catana and N. Navab. Compressive sensing in medical imaging: A review. *IEEE Transactions on Medical Imaging*, 32(4):678–697, 2013.

[31] V. Chan and A. Perlas. Basics of ultrasound imaging. In *Atlas of Ultrasound-Guided Procedures in Interventional Pain Management*, pages 13–19, 2011.

[32] L. Chen and et al. Direct comparison of pet/ct and mri to predict the pathological response to neoadjuvant chemotherapy in breast cancer: a meta-analysis. *Scientific reports*, 7(1):8479, 2017.

[33] K. Y. Cheng, S. Jerban, W. C. Bae, and et al. High-field mri advantages and applications in rheumatology. *Radiologic Clinics*, 62(5):837–847, 2024.

[34] W. Cheng, Y. Wang, H. Li, and et al. Learned full-sampling reconstruction from incomplete data. *IEEE Transactions on Computational Imaging*, 6:945–957, 2020.

[35] H. Y. Cho and et al. Pet/mri: A new frontier in molecular imaging. *Journal of Nuclear Medicine*, 56(2):22S–41S, 2015.

[36] M. H. Choi, B. Kim, D. Han, and et al. Compressed sensing for breath-hold high-resolution hepatobiliary phase imaging: image noise, artifact, biliary anatomy evaluation, and focal lesion detection in comparison with parallel imaging. *Abdominal Radiology*, pages 1–10, 2022.

[37] R. R. Coifman, Y. Meyer, S. Quake, and et al. Signal processing and compression with wavelet packets. *Wavelets and their applications*, pages 363–379, 1994.

[38] I. A. N. Cruz, L. M. Fayad, S. Ahlawat, and et al. Whole-body mri in musculoskeletal oncology: a comprehensive review with recommendations. *Radiology: Imaging Cancer*, 5(3):e220107, 2023.

[39] G. M. Currie and et al. Pet/mri, part 4: clinical applications. *Journal of nuclear medicine technology*, 50(2):90–96, 2022.

[40] G. M. Currie, P. Kamvosoulis, and S. Bushong. Pet/mri, part 2: technologic principles. *Journal of nuclear medicine technology*, 49(3):217–225, 2021.

[41] J. Czernin and M. E. Phelps. Positron emission tomography scanning: current and future applications. *Annual review of medicine*, 53(1):89–112, 2002.

[42] B. M. Dale, M. A. Brown, and R. C. Semelka. *MRI: basic principles and applications*. John Wiley & Sons, 2015.

[43] Centro de Desenvolvimento da Tecnologia Nuclear – CDTN. Bula para profissionais de saúde, 2017.

[44] G. Delso, S. Fürst, B. Jakoby, and et al. Performance measurements of the siemens mmr integrated whole-body pet/mr scanner. *Journal of nuclear medicine*, 52(12):1914–1922, 2011.

[45] G. Delso and S. Ziegler. Pet/mri system design. *European journal of nuclear medicine and molecular imaging*, 36:86–92, 2009.

[46] J. Van den Hoff. Principles of quantitative positron emission tomography. *Amino acids*, 29:341–353, 2005.

[47] R. K. G. Do and D. W. Dick. Pet/mri: safety considerations. *PET/MRI in Oncology: Current Clinical Applications*, pages 115–130, 2018.

[48] J. Dong and Y. Zheng. Compressed sensing algorithms applied to ill-posed ct image reconstructions. In *2023 Asia Symposium on Image Processing (ASIP)*, pages 79–86, 2023.

[49] H. Duan and et al. Reduced acquisition time per bed position for pet/mri using 68ga-rm2 or 68ga-psma-11 in patients with prostate cancer: a retrospective analysis. *American Journal of Roentgenology*, 218(2):333–340, 2022.

[50] M. J. Ehrhardt, K. Thielemans, L. Pizarro, and et al. Joint reconstruction of pet-mri by exploiting structural similarity. *Inverse Problems*, 31(1):015001, 2014.

[51] J. Erkin and C. G. Soares. Pet/mri: Clinical applications. 2016.

[52] L. Evangelista and et al. Clinical application of pet/mri. *Radiology-Nuclear Medicine Diagnostic Imaging: A Correlative Approach*, pages 788–813, 2023.

[53] W. P. Fendler and et al. Variations in pet/mri operations: Results from an international survey among 39 active sites. *Journal of Nuclear Medicine*, 57(12):2016–2021, 2016.

[54] J. A. Fessler and P. A. Balter. Compressed sensing in pet imaging. *IEEE Transactions on Medical Imaging*, 31(8):1508–1522, 2012.

[55] M. Fornasier and H. Rauhut. Compressive sensing. *Handbook of mathematical methods in imaging*, 1:187–229, 2015.

[56] N. Fuin, O. A. Catalano, M. Scipioni, and et al. Concurrent respiratory motion correction of abdominal pet and dynamic contrast-enhanced–mri using a compressed sensing approach. *Journal of Nuclear Medicine*, 59(9):1474–1479, 2018.

[57] M. C. M. Gammel and et al. A clinical role of pet-mri in prostate cancer? In *Seminars in Nuclear Medicine*, volume 54, pages 132–140. Elsevier, 2024.

[58] Y. Garcia, C. Franco, and C. J. Miosso. Method for improved image reconstruction in computed tomography and positron emission tomography, based on compressive sensing with prefiltering in the frequency domain. pages 2019–2025, 2020.

[59] P. Garg, R. Gosling, P. Swoboda, and et al. Cardiac magnetic resonance identifies raised left ventricular filling pressure: prognostic implications. *European Heart Journal*, 43(26):2511–2522, 2022.

[60] S. Gatidis, B. Bender, M. Reimold, and et al. Pet/mri in children. *European Journal of Radiology*, 94:A64–A70, 2017.

[61] J. Grandinetti, Y. Gao, Y. Gonzalez, and et al. Mr image reconstruction from undersampled data for image-guided radiation therapy using a patient-specific deep manifold image prior. *Frontiers in oncology*, 12:1013783–1013783, 2022.

[62] A. Granov, L. Tiutin, and T. Schwarz. *Positron emission tomography*. Springer Science & Business Media, 2013.

[63] R. Grazioso and M. Aykac. Pet imaging system with apd-based pet detectors and three-dimensional positron-confining magnetic field. (7,759,647).

[64] R. Grazioso, N. Zhang, J. Corbeil, and et al. Apd-based pet detector for simultaneous pet/mr imaging. *Nuclear Instruments and Methods in Physics Research Section A: Accelerators, Spectrometers, Detectors and Associated Equipment*, 569(2):301–305, 2006.

[65] E. Grober, R. B. Lipton, R. A. Sperling, and et al. Associations of stages of objective memory impairment with amyloid pet and structural mri: the a4 study. *Neurology*, 98(13):e1327–e1336, 2022.

[66] K. Guo, J. Wang, Z. Wang, and et al. Morphometric analysis program and quantitative positron emission tomography in presurgical localization in MRI-negative epilepsies: a simultaneous PET/MRI study. *European Journal of Nuclear Medicine and Molecular Imaging*, 49(6):1930–1938, 2022.

[67] D. G. Hampton and et al. Metabolic magnetic resonance imaging in neuroimaging: Magnetic resonance spectroscopy, sodium magnetic resonance imaging and chemical exchange saturation transfer. *Seminars in Ultrasound, CT and MRI*, 42(5):452–462, 2021. Advances in Neuroradiology I.

[68] D. G. Hampton and et al. Metabolic magnetic resonance imaging in neuroimaging: Magnetic resonance spectroscopy, sodium magnetic resonance imaging and chemical exchange saturation transfer. *Seminars in Ultrasound, CT and MRI*, 42(5):452–462, 2021. Advances in Neuroradiology I.

[69] K. M. Hanson. *Bayesian and related methods in image reconstruction from incomplete data*. Academic Press, 1987.

[70] B. A. Hargreaves, P. W. Worters, K. B. Pauly, and et al. Metal-induced artifacts in mri. *American Journal of Roentgenology*, 197(3):547–555, 2011.

[71] N. Hashemi, S. Masoudnia, A. Nejad, and et al. A memory-efficient deep framework for multi-modal mri-based brain tumor segmentation. In *2022 44th Annual International Conference of the IEEE Engineering in Medicine and Biology Society (EMBC)*, pages 3749–3752, 2022.

[72] P. Herscovitch. Principles of positron emission tomography. In *Functional Imaging in Movement Disorders*, pages 1–46. Crc Press, 2019.

[73] M. Hofmann, B. Pichler, B. Schölkopf, and et al. Towards quantitative pet/mri: a review of mr-based attenuation correction techniques. *European journal of nuclear medicine and molecular imaging*, 36:93–104, 2009.

[74] J. P. Hornak. *The basics of MRI*. Rochester Institute of Technology, 1996.

[75] G. N. Hounsfield. Computerized transverse axial scanning (tomography): Part 1. description of system. *The British journal of radiology*, 46(552):1016–1022, 1973.

[76] J. Hsieh. *Computed Tomography: Principles, Design, Artifacts, and Recent Advances*. SPIE Press, 2003.

[77] S. Huang, D. Savic, J. Yang, and et al. The effect of magnetic field on positron range and spatial resolution in an integrated whole-body time-of-flight pet/mri system. In *2014 IEEE Nuclear Science Symposium and Medical Imaging Conference (NSS/MIC)*, pages 1–4. IEEE, 2014.

[78] M. S. Igra, D. Paling, M. Wattjes, and et al. Multiple sclerosis update: use of mri for early diagnosis, disease monitoring and assessment of treatment related complications. *The British journal of radiology*, 90(1074):20160721, 2017.

[79] I. Irawati, S. Hadiyoso, G. Budiman, and et al. A novel texture extraction-based compressive sensing for lung cancer classification. *Journal of medical signals and sensors*, 12(4):278–284, 2022.

[80] H. Jadvar and P. M. Colletti. Competitive advantage of pet/mri. *European journal of radiology*, 83(1):84–94, 2014.

[81] A. Jalal, M. Arvinte, G. Daras, and et al. Robust compressed sensing mri with deep generative priors. *Advances in Neural Information Processing Systems*, 34:14938–14954, 2021.

[82] J. Jin and A. Rahme. Compressive sensing for medical imaging. In *Medical Image Processing: Principles and Applications*, pages 301–335. Elsevier, 2014.

[83] B. Johnson, H. Alizai, and M. Dempsey. Fast field echo resembling a ct using restricted echo-spacing (fracture): a novel mri technique with superior bone contrast. *Skeletal Radiology*, 50:1705–1713, 2021.

[84] F. D. Juengling, F. Wuest, S. Kalra, and et al. Simultaneous pet/mri: The future gold standard for characterizing motor neuron disease—a clinico-radiological and neuroscientific perspective. *Frontiers in Neurology*, 13:890425, 2022.

[85] J. H. Jung, Y. Choi, and K. C. Im. Pet/mri: technical challenges and recent advances. *Nuclear medicine and molecular imaging*, 50:3–12, 2016.

[86] P. Kamvosoulis and G. M. Currie. Pet/mri, part 1: establishing a pet/mri facility. *Journal of Nuclear Medicine Technology*, 49(2):120–125, 2021.

[87] R. Kang, D. Ai, G. Qu, and et al. Prior information constrained alternating direction method of multipliers for longitudinal compressive sensing mr imaging. *Neurocomputing*, 376:128–140, 2020.

[88] G. Katti, S. A. Ara, and A. Shireen. Magnetic resonance imaging (mri)–a review. *International journal of dental clinics*, 3(1):65–70, 2011.

[89] R. Kazimierczyk, K. A. Kaminski, and S. G. Nekolla. Cardiac pet/mri: Recent developments and future aspects. *Seminars in Nuclear Medicine*, 54(5):733–746, 2024.

[90] B. Kelly, T. P. Matthews, and M. A. Anastasio. Deep learning-guided image reconstruction from incomplete data. *arXiv preprint arXiv:1709.00584*, 2017.

[91] M. Kirienko, P. A. Erba, A. Chiti, and et al. Hybrid pet/mri in infection and inflammation: an update about the latest available literature evidence. *Seminars in Nuclear Medicine*, 53(1):107–124, 2023.

[92] V. Kuperman. *Magnetic resonance imaging: physical principles and applications*. Elsevier, 2000.

[93] T. Kustner, C. Wurslin, H. Schmidt, and et al. Combining compressed sensing with motion correction in acquisition and reconstruction for pet/mr. pages 788–792, 2015.

[94] A. Laakso and et al. Pet/mri for diagnosis and therapy monitoring in oncology. *European Journal of Nuclear Medicine and Molecular Imaging*, 42(12):1881–1893, 2015.

[95] C. N. Ladefoged, A. E. Hansen, O. M. Henriksen, and et al. Ai-driven attenuation correction for brain pet/mri: Clinical evaluation of a dementia cohort and importance of the training group size. *NeuroImage*, 222:117221, 2020.

[96] C. N. Ladefoged and A. B. Olin. Chapter 19 - pet/mri attenuation correction. pages 393–422. Academic Press, 2022.

[97] P. Lambin, R. T. H. Leijenaar, T. M. Deist, and et al. Radiomics: the bridge between medical imaging and personalized medicine. *Nature reviews Clinical oncology*, 14(12):749–762, 2017.

[98] K. Lameka, M. D. Farwell, and M. Ichise. Positron emission tomography. *Handbook of clinical neurology*, 135:209–227, 2016.

[99] P. C. Lauterbur. Image formation by induced local interactions: examples employing nuclear magnetic resonance. *nature*, 242(5394):190–191, 1973.

[100] J. H. Lee and et al. Deep learning for pet/mri image reconstruction: A review. *Physics in Medicine and Biology*, 67(18):18TR01, 2022.

[101] J. S. Lee. A review of deep-learning-based approaches for attenuation correction in positron emission tomography. *IEEE*, 5(2):160–184, 2021.

[102] S. Lenka, S. K. Pradhan, S. Mishra, and et al. A fractal based machine intelligence approach for the classification of brain tumor magnetic resonance imaging images. *NeuroQuantology*, 20(9):742–749, 2022.

[103] Z. Liang and P. C. Lauterbur. *Principles of magnetic resonance imaging*. SPIE Optical Engineering Press Bellingham, 2000.

[104] X. Ling, C. Yang, and H. Pei. Compressed video sensing network based on alignment prediction and residual reconstruction. In *2020 IEEE International Conference on Multimedia and Expo (ICME)*, pages 1–6, 2020.

[105] Y. Liu and et al. Deep learning-based correction of pet attenuation artifacts in simultaneous pet/mri. *Physics in Medicine and Biology*, 67(7):075007, 2022.

[106] M. Lustig, D. L. Donoho, and J. M. Pauly. Sparse mri: The application of compressed sensing for rapid mr imaging. *Magnetic Resonance in Medicine*, 58(6):1182–1195, 2007.

[107] J. E. Mackewn, J. Stirling, S. Jeljeli, and et al. Practical issues and limitations of brain attenuation correction on a simultaneous pet-mr scanner. *EJNMMI physics*, 7(24):1–17, 2020.

[108] K. Malczewski. Super-resolution with compressively sensed mr/pet signals at its input. *Informatics in Medicine Unlocked*, 18:100302, 2020.

[109] M. E. Mayerhoefer and et al. Mri and pet/mri in hematologic malignancies. *Journal of Magnetic Resonance Imaging*, 51(5):1325–1335, 2020.

[110] M. E. Mayerhoefer, H. Prosch, and L. Beer. Pet/mri versus pet/ct in oncology: a prospective single-center study of 330 examinations focusing on implications for patient management and cost considerations. *Springerlink*, 47(1):51–60, 2019.

[111] K. L. McMahon, G. Cowin, and G. Galloway. Magnetic resonance imaging: the underlying principles. *journal of orthopaedic & sports physical therapy*, 41(11):806–819, 2011.

[112] A. Mehranian, M. A. Belzunce, C. Prieto, and et al. Synergistic pet and sense mr image reconstruction using joint sparsity regularization. *IEEE transactions on medical imaging*, 37(1):20–34, 2017.

[113] B. G. Mersereau. *MRI-Guided and Compressed Sensing Reconstruction Methods for PET/MRI.* Doctoral dissertation, Graduate Faculty of North Carolina State University, 2017.

[114] M. Milà-Alomà, A. Brinkmalm, N. J. Ashton, and et al. Csf synaptic biomarkers in the preclinical stage of alzheimer disease and their association with mri and pet: a cross-sectional study. *Neurology*, 97(21):e2065–e2078, 2021.

[115] C. J. Miosso. *Compressive sensing with prior information applied to magnetic resonance imaging.* doctoral dissertation, Department of Electrical and Computer Engineering, The University of Texas at El Paso, 2010.

[116] C. J. Miosso, R. von Borries, M. Argaez, and et al. Compressive sensing reconstruction with prior information by iteratively reweighted least-squares. *IEEE Transactions on Signal Processing*, 57(6):2424–2431, 2009.

[117] C. J. Miosso, R. von Borries, and J. H. Pierluissi. Compressive sensing with prior information: Requirements and probabilities of reconstruction in l1-minimization. *IEEE Transactions on Signal Processing*, 61(9):2150–2164, 2012.

[118] C. J. Miosso, R. von Borries, and J. H. Pierluissi. Compressive sensing with prior information: Requirements and probabilities of reconstruction in l1 -minimization. *IEEE transactions on signal processing*, 61(9):2150–2164, 2013.

[119] G. A. L. Misned, H. M. H. Zakaly, F. T. Ali, and et al. A closer look at the efficiency calibration of labr3 (ce) and nai (tl) scintillation detectors using mcnpx for various types of nuclear investigations. *Heliyon*, 8(10), 2022.

[120] S. K. Mitra. *Digital Signal Processing: A Computer-Based Approach*. McGraw-Hill Higher Education, 2nd edition, 2001.

[121] R. Monika and S. Dhanalakshmi. An efficient medical image compression technique for telemedicine systems. *Biomedical signal processing and control*, 80:104404, 2023.

[122] J. F. C. Mota, N. Deligiannis, and M. R. D. Rodrigues. Compressed sensing with prior information: Strategies, geometry, and bounds. *IEEE Transactions on Information Theory*, 63(7):4472–4496, 2017.

[123] N. Motamedi, M. Revheim, T. Werner, and et al. Pet imaging in pediatric oncology: A narrative review. *Journal of Nuclear Medicine*, 64(supplement 1):P1179–P1179, 2023.

[124] B. Mulgrew, P. Grant, and J. Thompson. Digital signal processing: concepts and applications. 2002.

[125] V. Murad and et al. Atlas and anatomy of pet/mri. In *Atlas and Anatomy of PET/MRI, PET/CT and SPECT/CT*, pages 1–52. Springer, 2022.

[126] S. Musafargani, K. K. Ghosh, S. Mishra, and et al. Pet/mri: a frontier in era of complementary hybrid imaging. *European journal of hybrid imaging*, 2(12):1–28, 2018.

[127] S. A. Najjar and et al. Pet/mri in neurology: A comprehensive review. *Journal of Nuclear Medicine*, 57(12):1865–1881, 2016.

[128] Y. Nan, Z. Yi, and C. Bingxia. Review of compressed sensing for biomedical imaging. In *2015 7th International Conference on Information Technology in Medicine and Education (ITME)*, pages 225–228. IEEE, 2015.

[129] E. Nevo, P. Kamvosoulis, and G. Currie. Pet/mri, part 3: protocols and procedures. *Journal of Nuclear Medicine Technology*, 50(1):17–24, 2022.

[130] R. Ni. Pet imaging in animal models of parkinson's disease. *Behavioural Brain Research*, 438:114174, 2023.

[131] R. Nutt and M. A. King. Pet/mri: A dream come true? *The Lancet*, 376(9742):1199–1209, 2010.

[132] I. Oksuz. Brain mri artefact detection and correction using convolutional neural networks. *Computer Methods and Programs in Biomedicine*, 199:105909, 2021.

[133] A. V. Oppenheim and A. S. Willsky. *Sinais e Sistemas*. Pearson Universidades, 2nd edition, 2010.

[134] S. J. Orfanidis. *Introduction to Signal Processing*. Prentice Hall, 1995.

[135] L. Pang, Z. Zhang, G. Liuand, and et al. Comparison of the accuracy of a deep learning method for lesion detection in pet/ct and pet/mri images. *Molecular Imaging and Biology*, 26(5):802–811, 2024.

[136] V. M. Patel, R. Maleh, A. C. Gilbert, and et al. Gradient-based image recovery methods from incomplete fourier measurements. *IEEE transactions on image processing*, 21(1):94–105, 2012.

[137] D. H. Paulus, H. Braun, B. Aklan, and et al. Simultaneous pet/mr imaging: Mr-based attenuation correction of local radiofrequency surface coils. *Medical physics (Lancaster)*, 39(7):4306–4315, 2012.

[138] C. Pedersen, M. Aboian, J. E. McConathy, and et al. Pet/mri in pediatric neuroimaging: Primer for clinical practice. *American Journal of Neuroradiology*, 2022.

[139] S. E. Poirier, B. Y. M. Kwan, M. T. Jurkiewicz, and et al. An evaluation of the diagnostic equivalence of 18f-fdg-pet between hybrid pet/mri and pet/ct in drug-resistant epilepsy: A pilot study. *Epilepsy Research*, 172:106583, 2021.

[140] J. P. T. Portillo. *Introducción a las señales y sistemas*. Universidad del Norte, 2016.

[141] J. G. Proakis and M. Salehi. *Fundamentals of Communication Systems*. Pearson Prentice Hall, 2nd edition, 2005.

[142] K. P. Pruessmann. Encoding and reconstruction in parallel mri. *NMR in biomedicine*, 19(3):288–299, 2006.

[143] J. Qi and et al. Bayesian joint reconstruction of pet and mr images using a unified emission-transmission model. *IEEE Transactions on Medical Imaging*, 29(11):1883–1898, 2010.

[144] A. Qiu, L. Xu, and C. Liu. Predicting diagnosis 4 years prior to alzheimer's disease incident. *NeuroImage: Clinical*, 34:102993, 2022.

[145] T. Rahim, L. Novamizanti, I. N. A. Ramatryana, and et al. Compressed medical imaging based on average sparsity model and reweighted analysis of multiple basis pursuit. *Computerized medical imaging and graphics*, 90:101927–101927, 2021.

[146] A. Rajagopal, A. P. Leynes, N. Dwork, and et al. Physics-driven deep learning for pet/mri. *arXiv preprint arXiv:2206.06788*, 2022.

[147] A. Renner, I. Rausch, J. C. Gonzalez, and et al. Technical note: A pet/mr coil with an integrated, orbiting 511 kev transmission source for pet/mr imaging validated in an animal study. *Medical physics (Lancaster)*, 49(4):2366–2372, 2022.

[148] A. O. Rodriguez. Principles of magnetic resonance imaging. *Revista mexicana de física*, 50(3):272–286, 2004.

[149] W. C. Röntgen. On a new kind of rays. *Science*, 3(59):227–231, 1896.

[150] A. B. Rosenkrantz, K. Friedman, H. Chandarana, and et al. Current status of hybrid pet/mri in oncologic imaging. *American journal of roentgenology*, 206(1):162–172, 2016.

[151] T. D. Ruddy, M. Al-Mallah, J. A. Arrighi, and et al. Snmmi/acr/asnc/scmr joint credentialing statement for cardiac pet/mri: endorsed by the american heart association. *Circulation: Cardiovascular Imaging*, 15(8):e014576, 2022.

[152] B. Saboury, M. A. Parsons, M. Moghbel, and et al. Quantification of aging effects upon global knee inflammation by 18F-FDG-PET. *Nuclear Medicine Communications*, 37(3):254–258, 2016.

[153] H. Schöder, Y. E. Erdi, S. M. Larson, and et al. Pet/ct: a new imaging technology in nuclear medicine. *European journal of nuclear medicine and molecular imaging*, 30:1419–1437, 2003.

[154] R. Schofield, L. Menezes, and S. R. Underwood. Nuclear cardiology: state of the art. *Heart*, 107(12):954–961, 2021.

[155] Z. Sedlakova, I. Nachtigalova, R. Rusina, and et al. Alzheimer 's disease identification from 3D SPECT brain scans by variational analysis. *Biomedical Signal Processing and Control*, 80:104385, 2023.

[156] J. A. Seibert. X-ray imaging physics for nuclear medicine technologists. part 1: Basic principles of x-ray production. *Journal of Nuclear Medicine Technology*, 32(3):139–147, 2004.

[157] W. Sensakovic, S. Armato III, A. Starkey, and et al. Automated lung segmentation of diseased and artifact-corrupted magnetic resonance sections. *Medical physics*, 33:3085–93, 10 2006.

[158] T. Sepehrizadeh, I. Jong, M. DeVeerand, and et al. Pet/mri in paediatric disease. *European journal of radiology*, 144:109987, 2021.

[159] K. R. Sewell, S. R. Rainey-Smith, V. L. Villemagne, and et al. The interaction between physical activity and sleep on cognitive function and brain beta-amyloid in older adults. *Behavioural Brain Research*, 437:114108, 2023.

[160] C. E. Shannon. Communication in the presence of noise. *Proceedings of the IRE*, 37(1):10–21, 1949.

[161] K. K. Shung, M. Smith, and B.M.W. Tsui. *Principles of Medical Imaging*. Academic Press, 2012.

[162] O. P. Shvaika and A. P. Grekov. Scintillators and scintillation materials, 1963.

[163] G. B. Silva. *Avaliação de extração de informação a priori entre imagens de diferentes modalidades para aprimoramento de reconstrução de imagens médicas em equipamentos de PET-MRI*. Trabalho de conclusão de curso, Graduação em Engenharia Eletrônica, Universidade de Brasília, Campus Gama, 2020.

[164] A. Singnurkar and et al. Head-to-head comparison of the diagnostic performance of fdg pet/ct and fdg pet/mri in patients with cancer: a systematic review and meta-analysis. *American Journal of Roentgenology*, 223(3):e2431519, 2024.

[165] A. Smeraldo, A. M. Ponsiglione, A. Soricelli, and et al. Update on the use of pet/mri contrast agents and tracers in brain oncology: A systematic review. *International Journal of Nanomedicine*, 17:3343, 2022.

[166] V. P. Sudarshan, G. F. Egan, Z. Chen, and et al. Joint pet-mri image reconstruction using a patch-based joint-dictionary prior. *Medical image analysis*, 62:101669, 2020.

[167] C. J. Sunderland, M. Steiert, J. E. Talmadge, and et al. Targeted nanoparticles for detecting and treating cancer. *Drug Development Research*, 67(1):70–93, 2006.

[168] C. Tang, J. Chen, K. Shao, and et al. Blunt dopamine transmission due to decreased GDNF in the PFC evokes cognitive impairment in Parkinson's disease. *Neural Regeneration Research*, 18(5):14789–14800, 2023.

[169] X. Tao, S. Li, Z. Zhang, and et al. Prior-information-based remote sensing image compression with bayesian dictionary learning. In *2017 IEEE 85th Vehicular Technology Conference (VTC Spring)*, pages 1–6. IEEE, 2017.

[170] S. Thirumurugan, P. Dash, X. Liu, and et al. Angiopep-2-decorated titanium–alloy core–shell magnetic nanoparticles for nanotheranostics and medical imaging. *Nanoscale*, 14(39):14789–14800, 2022.

[171] D. W. Townsend and et al. Physical principles and technology of clinical pet imaging. *Annals-Academy of Medicine Singapore*, 33(2):133–145, 2004.

[172] S. T. Treves and M. Pomper. Pet/mri: A review of the clinical literature. *Journal of Nuclear Medicine*, 51(12):182–1834, 2010.

[173] R. M. van Geuns, P. A. Wielopolski, H. G. de Bruin, and et al. Basic principles of magnetic resonance imaging. *Progress in cardiovascular diseases*, 42:149–156, 1999.

[174] R. M. van Geuns, P. A. Wielopolski, H. G. de Bruin, and et al. Basic principles of magnetic resonance imaging. *Progress in cardiovascular diseases*, 42(2):149–156, 1999.

[175] S. Vandenberghe and P. K. Marsden. Pet-mri: a review of challenges and solutions in the development of integrated multimodality imaging. *Physics in Medicine & Biology*, 60(4):R115, 2015.

[176] J. J. Vaquero and P. Kinahan. Positron emission tomography: current challenges and opportunities for technological advances in clinical and preclinical imaging systems. *Annual review of biomedical engineering*, 17(1):385–414, 2015.

[177] P. Veit-Haibach, H. Ahlström, R. Boellaard, and et al. International eanm-snmmi-ismrm consensus recommendation for pet/mri in oncology. *European journal of nuclear medicine and molecular imaging*, 50(12):3513–3537, 2023.

[178] T. Vitor, K. M. Martins, T. M. Ionescu, and et al. Pet/mri: a novel hybrid imaging technique. major clinical indications and preliminary experience in brazil. *Einstein (São Paulo)*, 15:115–118, 2017.

[179] J. Vivian. *Compressive sensing using directional filters for Magnetic Resonance Image reconstruction under different k-space trajectories.* Dissertação de mestrado, Programa de Pós-Graduação em Engenharia Biomédica, Universidade de Brasília, Campus Gama, 2020.

[180] R. von Borries, C. J. Miosso, and C. Potes. Compressed sensing using prior information. In *2007 2nd IEEE International Workshop on Computational Advances in Multi-Sensor Adaptive Processing*, pages 121–124. IEEE, 2007.

[181] S. S. Vulasala, M. Virarkar, N. Karbasian, and et al. Whole-body mri in oncology: A comprehensive review. *Clinical Imaging*, 108:110099, 2024.

[182] G. Wagenknecht, H. J. Kaiser, F. M. Mottaghy, and et al. Mri for attenuation correction in pet: methods and challenges. *Springerlink*, 26(1):99–113, 2012.

[183] C. Wahl and J. Schramm. Pet/mri: The holy grail of molecular imaging? *Journal of Nuclear Medicine*, 54(10):182S–189S, 2013.

[184] R. L. Wahl and J. W. Buchanan. Principles and practice of positron emission tomography. *Principles and Practice of Positron Emission Tomography (Lippincott, Williams and Wilkins, Philadelphia, PA, 2002)*, 2002.

[185] G. Wang and et al. A review of pet/mri reconstruction algorithms. *Physics in Medicine and Biology*, 65(1):01TR01, 2020.

[186] J. Wang and L. Maurer. Positron emission tomography: applications in drug discovery and drug development. *Current topics in medicinal chemistry*, 5(11):1053–1075, 2005.

[187] Q. Wang, X. Chen, M. Wei, and et al. Simultaneous encryption and compression of medical images based on optimized tensor compressed sensing with 3d lorenz. *Biomedical engineering online*, 15(1):118–118, 2016.

[188] Y. Wang, X. Zhang, D. Li, and et al. A global decoupling control algorithm for lc-dm adaptive optics system. *IEEE Access*, 9:142302–142313, 2021.

[189] T. Wech, K. P. Kunze, C. Rischpler, and et al. A compressed sensing accelerated radial ms-caipirinha technique for extended anatomical coverage in myocardial perfusion studies on pet/mr systems. *Physica Medica*, 64:157–165, 2019.

[190] M. Weiger and K. P. Pruessmann. Short-t2 mri: Principles and recent advances. *Progress in nuclear magnetic resonance spectroscopy*, 114:237–270, 2019.

[191] J. Wen and et al. High-quality fusion and visualization for mr-pet brain tumor images via multi-dimensional features. *IEEE Transactions on Image Processing*, 2024.

[192] J. Won, J. Yeon, H. Park, , and et al. Development and initial results of a brain pet insert for simultaneous 7-tesla pet/mri using an fpga-only signal digitization method. *IEEE Transactions on Medical Imaging*, 40(6):1579–1590, 2021.

[193] J. Wu and et al. Joint reconstruction of pet and mr images using a unified framework. *IEEE Transactions on Medical Imaging*, 32(4):699–710, 2013.

[194] D. T. Wymer, H. P. Patel, W. F. Burke III, and et al. Phase-contrast mri: physics, techniques, and clinical applications. *Radiographics*, 40(1):122–140, 2020.

[195] Y. Xi, J. Zhao, J. R. Bennett, and et al. Simultaneous ct-mri reconstruction for constrained imaging geometries using structural coupling and compressive sensing. *IEEE Transactions on Biomedical Engineering*, 63(6):1301–1309, 2015.

[196] Y. Xie and Q. Li. A review of deep learning methods for compressed sensing image reconstruction and its medical applications. *Electronics*, 11(4):586, 2022.

[197] Z. Xie, T. Li, X. Zhang, and et al. Anatomically aided pet image reconstruction using deep neural networks. *Medical physics*, 48(9):5244–5258, 2021.

[198] S. Yamamoto, H. Watabe, Y. Kanai, and et al. Interference between pet and mri sub-systems in a silicon-photomultiplier-based pet/mri system. *Physics in Medicine & Biology*, 56(13):4147, 2011.

[199] J. Yang, D. Park, G. T. Gullberg, and et al. Joint correction of attenuation and scatter in image space using deep convolutional neural networks for dedicated brain 18 f-fdg pet. *IOP*, 64(7):075019–075019, 2019.

[200] M. Yaqub, F. Jinchao, K. Arshid, and et al. Deep learning-based image reconstruction for different medical imaging modalities. *Computational and mathematical methods in medicine*, 2022(1):1–18, 2022.

[201] C. Yuan, W. S. Kerwin, M. S. Ferguson, and et al. Contrast-enhanced high resolution mri for atherosclerotic carotid artery tissue characterization. *Journal of Magnetic Resonance Imaging: An Official Journal of the International Society for Magnetic Resonance in Medicine*, 15(1):62–67, 2002.

[202] H. Zaidi and A. Del Guerra. An outlook on future design of hybrid pet/mri systems. *Medical physics*, 38(10):5667–5689, 2011.

[203] M. Zhang, M. Li, J. Zhou, and et al. High-dimensional embedding network derived prior for compressive sensing mri reconstruction. *Medical Image Analysis*, 64:101717, 2020.

[204] M. Zhang, M. Zhang, F. Zhang, and et al. Robust brain mr image compressive sensing via re-weighted total variation and sparse regression. *Magnetic resonance imaging*, 85:271–286, 2022.

[205] T. Zheng, L. Liu, L. Li, and et al. Case report: Advantages of high-resolution mri in evaluating the efficacy of drug therapy for intracranial atherosclerotic plaques. *Frontiers in Aging Neuroscience*, 14:804074, 2022.

[206] S. I. Ziegler. Positron emission tomography: principles, technology, and recent developments. *Nuclear Physics A*, 752:679–687, 2005.